

**A Two Phase, Two Component Model  
for  
Natural Convection in a Porous Medium**

**by  
P.A. Forsyth and R.B. Simpson**

**Research Report CS-89-55  
November 1989**

# **A Two Phase, Two Component Model for Natural Convection in a Porous Medium**

P A Forsyth and R B Simpson

Department of Computer Science , University of Waterloo  
Waterloo, Ontario, Canada, N2L 3G1

## **Abstract**

A numerical study of natural convection in a two phase, two component flow in a porous medium heated from below is presented. Interphase mass and energy transfer, latent heat, and bouyancy effects are major physical features. This study extends earlier studies of natural convection based on single phase, saturated porous medium models. The appearance of two phase heat pipe zones in the flow have a marked effect on the fluid and heat flows as well as on the performance of numerical methods. The numerical techniques for handling phase change, Jacobian construction, and time step selection are discussed.

Keywords: two phase, porous medium, convection, heat pipe

## **Acknowledgement**

This work was supported by the government of Ontario through the Information Technology Research Centre, and by the Natural Science and Engineering Research Council of Canada.

## Introduction

The heat transfer across a layer of fluid in a porous medium which is heated from below has been extensively studied using a model based on a single liquid phase saturating the porous medium. From a heat transfer point of view, this model exhibits two basic regimes. The conductive regime at low bottom heating, in which the heat is transferred primarily by conduction, and the liquid's motion is absent or secondary, and the convective regime for higher bottom heating, in which the liquid flows in convection cells or irregular quasi periodic flows which are the primary mechanisms of heat transfer across the layer. The literature of this model is reviewed in § 1.2 below.

The validity of the single phase model becomes increasingly questionable with increasing bottom heating since for real fluids the higher temperatures may exceed the saturation temperature of the liquid phase, unless the layer is subjected to increasing pressure. In this paper, we extend these studies by employing a more complex model for the fluid which consists of two chemical components, water and air, and two physical phases, liquid and vapour. The model simulates the flow of fluid and energy through both the water saturated zone and the overlying unsaturated zone of a rock matrix uniformly heated from below. With the bottom temperature of the layer as the basic parameter of the study, the flow is studied dynamically, starting from a standard conductive state (properties varying with depth only.) Although the extended model poses a significantly larger computation than its single phase predecessor, the increased computing power provided by current developments in computational techniques as discussed in § 2, and in processors, make this model viable even for relatively inexpensive and commonly available workstations.

For the range of bottom heating used in our study, this model exhibits three heat transfer regimes, which have been identified in Hardee and Nilson<sup>12</sup>, 1977. The first two of these, in order of increasing bottom heating, are the conductive, and liquid phase convective regimes, in which the saturated zone has the characteristics of the single phase model discussed in the opening paragraph, modified in minor ways by the presence of the air. At higher bottom temperatures, however, the temperature locally in the flow field can rise to, and be limited by, the water saturation temperature at which the water component is partially evaporated and exists in a two phase state. Such two phase zones form locally in the liquid phase convection cells of the saturated zone, and limit their role in heat transfer while introducing a new heat transfer mechanism; which is a cycle of evaporation, vapour convection and condensation. This regime is referred to as the two phase convection regime. The

role of phase change in the heat and mass transfer by a volatile fluid has been studied under the name of the heat pipe effect. A prominent feature of heat pipes is a counter current flow between the two phases of one chemical component i.e. water. The vapour phase rises due to buoyancy, while the liquid phase sinks past it due to gravity. Previous work on heat pipe effects appears to have concentrated on experimental and analytical studies of one dimensional two phase zones, to predict transport rates, and the lengths of the two phase zones (see § 1.3 below.) A major feature of this study is the demonstration of the formation of localized two phase ‘pockets’ in the convection cells of the saturated zone, with general two dimensional shapes. These pockets are two dimensional heat pipes, and modeling a flow in which they develop requires a computational technique which can be applied uniformly and efficiently to both saturated and unsaturated zones.

§ 2 of the paper is devoted to the mathematical model, and the numerical solution strategies we have used to meet these challenges. The geometry and equations for the two phase, two component model are described in § 2.1. The layer is confined to a box 60 meters deep by 90 meters wide, and the rock matrix void is filled 2/3 with water and 1/3 with air. The top of the box is held at 20 °C, and the evolution of the dynamic model to a steady state for bottom temperatures in the range 70 °C to 150 °C has been computed.

The equations involve 8 state variables, with three evolutionary partial differential equations and five algebraic equations. The flow bed is discretized into square cells, and the equations are discretized in time by a fully implicit method, and in space by a conservative finite volume scheme, as discussed further in § 2.2. The resulting algebraic equations are solved by full Newton’s method, using a preconditioned conjugate residual iteration to solve the linear systems of equations. Numerical differentiation is used to produce an effective approximation to the Jacobian matrix for Newton’s method. In § 2.4, we discuss how the structure of the discretized conservation laws allow us to compute the Jacobian matrix very economically. This procedure also substantially simplifies the incorporation, or modification, of complex physical relationships for transport coefficients, or thermodynamics in the model. As a result, there is little reason for us to use simplifying assumptions, such as the Boussinesq approximation, in our computation.

The primary variables are the three state variables that are advanced in time by solving the discretized conservation laws. While two of these are always the pressure and the temperature, the goal of having a uniform computational technique for the

entire fluid is complicated by the fact that the third primary variable, for a given cell, depends on the liquid saturation condition of this cell. Accommodating phase changes at arbitrary locations in the flow field complicates the numerical procedure, basically because the nonlinear model equations do not have a reliable linearization in the presence of extensive phase changes. Emphasis should be placed on "changes" here, since it is not the presence of two phases in the flow that makes linearization difficult, but the possibility of phase change at physically realizable nearby flows that reduces the reliability of linearizations as needed for Newton's method. These computational difficulties underlie the discussions of primary variable selection and switching in § 2.5 and the time step selection strategy presented in § 2.6, as well as the discussion of § 4.1.

Useful summaries of the dynamical state of the flow are provided by the rates of heat transfer into the layer through the bottom  $Q_{\text{bot}}(t)$ , and out through the top,  $Q_{\text{top}}(t)$ . These symbols are defined more precisely in § 3. When the bottom heating is low enough that the layer remains in the conductive regime,  $Q_{\text{bot}}(t)$  and  $Q_{\text{top}}(t)$  approach each other monotonically. The development of convection cells in the liquid phase can be viewed as a dynamic instability of the conduction regime at higher bottom heating. The onset of this instability is clearly marked in the profile of  $Q_{\text{bot}}(t)$  by the start of a pulse, shown in the leading figure of § 3, as the layer takes in energy to drive the convection cell formation. The pulse in  $Q_{\text{bot}}(t)$  peaks and then it decays to the steady state, where it coincides with  $Q_{\text{top}}(t)$ . The physical mechanism of this pulse is explained in § 3.1. By contrast, the transition from the liquid phase convection regime to two phase convection regime is not reflected in these profiles. It is discussed in § 3.2 and is apparently of a different character than the instability that marks the transition from conductive to convective regimes.

Some concluding observations are made in § 4; the problems of controlling the time step and our approach to it are discussed in § 4.1, and in the following subsection the heat transfer characteristics of the extended model are described.

## § 1.2 Single Phase Studies

The heat transfer across a layer, heated from below, of a single liquid phase saturating a porous medium has been extensively studied and reported in the literature. The models employed usually incorporate the conservation of mass and of energy, Darcy's law for fluid flux and the Boussinesq approximation for buoyancy. The model equations are the evolutionary partial differential equations for the

stream function and for the temperature, and the flow is studied in an impermeable box with insulated side walls and isothermal top and bottom walls relative to gravity.

After non dimensionalizing, the temperature differential across the layer appears in the Rayleigh number parameter,  $R_a$ , of the temperature equation. Earlier studies of two dimensional flows in sealed boxes of rectangular cross section are referenced and reviewed in Caltagirone<sup>4</sup>, 1975, in the survey article by Combarous and Bories<sup>7</sup>, 1975, and, with applications to geothermal systems, in Cheng<sup>6</sup>, 1978.

The basic phenomenon of this literature for a horizontal layer is that as  $R_a$  increases past a critical Rayleigh number,  $R_a(crit)$ , solutions of the model equations corresponding to two dimensional convection cells, or rolls, bifurcate from the simple conduction solution. The convection cells transfer heat across the layer more efficiently than conduction alone, and the ratio of the heat transferred via the convection solution to that via conduction only is the Nusselt number. The above referenced literature studies the critical Rayleigh numbers, the influence of box geometry on it, the stability of the convection cells, and the corresponding heat transfer, summarized by graphs showing Nusselt number as a function of Rayleigh number.

The ‘sealed box’ model assumption of an impermeable top and bottom for the box containing the flow is central to the value, and even existence, of a critical Rayleigh number,  $R_a(crit)$ , above which the conduction solution loses stability and convection cells form. The influence of the boundary conditions on  $R_a(crit)$  for this simple model has been discussed in an early paper by Nield,<sup>17</sup>, 1968. Using a linearized stability analysis of the conduction state (i.e. isothermal top and bottom), Nield reproduced the earlier result that for fixed temperature boundaries at the top and bottom which are rigid to fluid motion  $R_a(crit)=4\pi^2$ . He further showed that, if the top layer is relaxed to allow a specified heat flux,  $R_a(crit)$  is reduced to 27.1, and if it is further relaxed to also allow a constant pressure upper surface the  $R_a(crit)$  is reduced to 9.87, ( $\pi^2$ ).

More recently, stability of the convection cells under the perturbing effect of tilting the layer relative to gravity has been studied in Moya and Ramos<sup>16</sup>, 1987 Sen, Vasseur, and Robillard<sup>23</sup>, 1987 and Caltagirone and Bories<sup>5</sup>, 1985. This latter reference analyses three dimensional convection cells, as well as two dimensional rolls.

The loss of stability of these cells through Hopf bifurcation to quasi periodic solutions, as  $R_a$  increases has also been studied in Caltagirone<sup>4</sup>, 1975, by Borkowska-Pawlak and Kordylewski<sup>3</sup>, 1982 and, more recently, as a study of the ‘cascading’ of bifurcations for very large Rayleigh numbers in Kimura, Schubert, and Straus<sup>14</sup>, 1986.

In Rao, Fukuda and Hasegawa<sup>20</sup>, 1988, this line of study is extended to a more complex geometry, by studying cellular flows in a horizontal annulus. In a study that is directed towards modeling geophysical gas dynamics, Davidson<sup>8</sup>, 1986, computed the stability of the formation of a single convection cell in the vapour phase of a porous flow that overlies a liquid pool with an isothermal surface.

These references have in common that they are studies of the formation of cellular convective flows in a single saturating phase under buoyant heating, and that they employ the stream function, temperature pair of partial differential equations as the basic mathematical model. This pair of equations reflect linear, constant coefficient material properties, except for the nonlinearity associated with the buoyant convection coupling terms.

More physical features are present in the multicomponent, single phase model of Lai, Bodvarsson, and Witherspoon<sup>15</sup>, 1986 based on three transport equations for three model variables, pressure, temperature, and concentration of a chemical species. Saturated zone flow dynamics are computed by the coupled pressure and temperature equations, and the transport of the passive chemical component is included. Operator splitting of diffusive and convective transport is used, which allows careful consideration of errors due to discretization of the convective transport terms. It also permits the implicit equation solving to be limited to the diffusive transport terms, which are basically linear. Among the numerical tests reported in this paper, is a study of a thermal cell in a porous slab driven by sidewall heating, for Rayleigh numbers in the range 25 to 200, which exhibits strong convection at the upper end of this range.

### § 1.3 Multiphase Review

Two departures from the relatively simple equations used for the models for the studies of § 1.2 will be reviewed in this section: the inclusion of phase change for the fluid, which introduces additional variables and algebraic thermodynamic equations and constraints; and the inclusion of unsaturated flows, which introduces nonlinear permeabilities, as well as additional variables and equations.

Two papers from 1977, Sondergeld and Turcotte<sup>25</sup>, and Hardee and Nilson<sup>12</sup> provide qualitative and experimental insights into some implications of phase change for the flow. In the first of these, the authors report on experiments in which a water saturated layer in a bed of sand was heated from below to form a two phase zone. Their study reports the formation of convection cells in a saturated liquid zone, like those referred to in the above review of single phase flows, above a hot two phase zone.

The paper observes that: "The two phase region was of variable geometry and had a distinctly non horizontal steam-water interface with the overlying water zone. Convective instabilities were initiated by the occurrence of the phase change". The paper concludes with a discussion of applications to explaining geological formations. The question of the stability of a two phase zone below a liquid saturated zone which is raised in Sondergeld and Turcotte is also addressed by Schubert and Straus<sup>22</sup>, 1980. The authors discuss configurations of geothermal fields, present a linearized stability analysis of two horizontal layers, the lower being a two phase zone, and conclude that such layers can be stable for sufficiently small permeabilities.

In a study motivated by modeling nuclear reactor accidents, Hardee and Nilson<sup>12</sup> identify qualitatively three heat transfer regimes closely connected with those discussed in this paper, and derive algebraic relations for the heat transfer parameters based on macroscopic heat and mass balance arguments for a single convection cell, with internal heating of the fluid. Although a major contribution of the paper is its reporting of experimental results, these are not closely related to this study since they are carried out in a cylindrical apparatus, with heat generation distributed in the flow field, and in a high permeability medium.

Experimental measurements of the characteristics of heat pipes, and one dimensional models for them are reported in Bau and Torrance<sup>1</sup>, 1982 and in Udell<sup>28</sup>, 1985 based on cylindrical apparatus. The former paper reports long term fluctuations in the temperature profile in the two phase zone underlying a liquid saturated layer, suggesting that the two phase zone may not have a stable steady state, but may have a stable periodic or quasi periodic state. The authors also point out that the overlying saturated layer can be viewed as a single phase layer heated from below as discussed in the previous section. However, permeable, constant pressure boundary conditions are more appropriate than 'sealed box' impermeable



boundaries for this context, and as mentioned in § 1.2<sup>17</sup> such a layer is unstable, i.e. develops convective solutions, for any temperature differential across it.

The mathematical analyses of these heat pipe flows have been carried out using one dimensional models for the counter current flows of the two phases of a single saturating component (water), and analytical derivations of model properties.

Two dimensional mathematical models which are similar to those presented in § 2.1 below have been used to study the evolution of the unsaturated porous flow field about a nuclear waste repository by Pollock<sup>18</sup> , 1986, and by Tsang and Pruess<sup>27</sup> , 1987. Two phase multi-component models are used in the simulation of geothermic fields, where, typically, the dynamic effect of a well bore on a flow field is studied; see the survey article by Pruess<sup>19</sup> ,1990, and its bibliography.

We can identify , and distinguish, the role of this study in relation to those reviewed above by noting that we are studying the stability and heat transfer phenomena of the formation of convection cells under buoyant heating which is the subject of the single phase studies reviewed in § 1.2. However, instead of the stream function, temperature pair of equations appropriate to the single phase models used in those studies, we are using the extended equations for multiphase multicomponent flows. I.e. the primitive variable transport equations are solved, in conjunction with the algebraic relations and constraints governing two chemical components and the thermodynamics of phase change, which allows a uniform treatment of saturated and unsaturated zones. These equations admit of the phenomena of the modeling described in § 1.3; in particular, the formation of heat pipes. They do, however, pose numerical solution difficulties beyond those of the simpler equations of § 1.2, and which are discussed in detail in the sequel.

## 2. The Mathematical Model

The following glossary of symbols will be used to describe the mathematical model:

where:

$S_m$	=	saturation of phase $m = \ell, g$ (liquid, gas)
$P$	=	pressure [Kpa]
$T$	=	temperature [ $^{\circ}K$ ]
$K$	=	absolute permeability [ $m^2$ ]
$K_{rm}$	=	relative permeability of phase $m$
$\mu_m$	=	viscosity of phase $m$ [Kpa-day]
$U_m$	=	internal energy of phase $m$ [J/mole] ( $r = \text{rock}$ )
$h_m$	=	enthalpy of phase $m$ [J/mole]
$M_m$	=	molar density of phase $m$ [mole/ $m^3$ ]
$\phi$	=	porosity
$\lambda_H$	=	composite heat conductivity [J/( $m$ -day- $^{\circ}K$ )]
$D_g$	=	gas phase diffusivity [ $m^2$ /day]
$\rho_m$	=	mass density of phase $m$ [Kg/ $m^3$ ]
$g$	=	acceleration due to gravity [ $m/sec^2$ ]
$d$	=	depth [ $m$ ]
$Y_p$	=	mole fraction of component $p$ in the gas phase
$X_p$	=	mole fraction of component $p$ in the liquid phase

These symbols can be divided into variables for which the evolution is to be computed by the model, and parameters, including possibly nonlinear functions, which are to be specified for the model. The variables are:

$$S_g, S_{\ell}, X_a, X_w, Y_a, Y_w, P, T$$

and the parameters and their specifications are given in Appendix A.

For the description of the conservation laws of the model, it is convenient to combine the mechanical driving forces of pressure and buoyancy for the liquid and gas phases into phase potentials. The gradients of these potentials are defined by

$$\nabla \psi_{\ell} = \nabla P - \rho_{\ell} g \nabla d$$

$$(2.1) \quad \nabla \psi_g = \nabla P - \rho_g g \nabla d$$

We have assumed here that the capillary pressure ( $P_\ell - P_g$ ) is small, and consequently,  $P_\ell = P_g = P$  is a satisfactory modeling approximation. Following Forsyth, 1990<sup>10</sup> and using the phase potentials of (2.1), the basic conservation equations, based on the multiphase form of Darcy's law, can be written

Conservation of air:

$$(2.2) \quad \begin{aligned} & \frac{\partial}{\partial t} (\phi [S_\ell M_\ell X_a + S_g M_g Y_a]) \\ &= \nabla \cdot \left\{ M_\ell X_a \frac{K K_{r\ell}}{\mu_\ell} \nabla \psi_\ell \right\} \\ &+ \nabla \cdot \left\{ M_g Y_a \frac{K K_{rg}}{\mu_g} \nabla \psi_g \right\} \\ &+ \nabla \cdot \{ D_g M_g \nabla Y_a \} \end{aligned}$$

Conservation of water:

$$(2.3) \quad \begin{aligned} & \frac{\partial}{\partial t} (\phi [S_\ell M_\ell X_w + S_g M_g Y_w]) \\ &= \nabla \cdot \left\{ M_\ell X_w \frac{K K_{r\ell}}{\mu_\ell} \nabla \psi_\ell \right\} \\ &+ \nabla \cdot \left\{ M_g Y_w \frac{K K_{rg}}{\mu_g} \nabla \psi_g \right\} \\ &+ \nabla \cdot \{ D_g M_g \nabla Y_w \} \end{aligned}$$

Conservation of energy:

$$(2.4) \quad \begin{aligned} & \frac{\partial}{\partial t} (\phi [S_\ell M_\ell U_\ell + S_g M_g U_g] \\ &+ (1 - \phi) U_r M_r) \\ &= \nabla \cdot \left\{ h_\ell M_\ell \frac{K K_{r\ell}}{\mu_\ell} \nabla \psi_\ell \right\} \\ &+ \nabla \cdot \left\{ h_g M_g \frac{K K_{rg}}{\mu_g} \nabla \psi_g \right\} \end{aligned}$$

$$\begin{aligned}
 & + \nabla \cdot \{D_g M_g h_{gw} \nabla Y_w\} \\
 & + \nabla \cdot \{D_g M_g h_{ga} \nabla Y_a\} \\
 & + \nabla \cdot \lambda_H \nabla T
 \end{aligned}$$

In addition to these conservation laws, equilibrium thermodynamics determines the following two relations

$$(2.5) \quad Y_a = Z_a(P, T)X_a, \quad Y_w = Z_w(P, T)X_w$$

The functional dependence of  $Z_a$  and  $Z_w$  on P and T is given in Appendix A.

For each of the three physically meaningful phase states that the model fluid can take on, the model variables must satisfy the corresponding equations and inequalities.

(2.6a) the liquid saturated state

$$S_\ell = 1, S_g = 0, X_a + X_w = 1, Y_a + Y_w \leq 1$$

(2.6b) the vapour - liquid mixed state

$$S_g + S_\ell = 1, X_a + X_w = 1, Y_a + Y_w = 1, S_\ell > 0, S_g > 0$$

(2.6c) the gas saturated state

$$S_\ell = 0, S_g = 1, Y_a + Y_w = 1, X_a + X_w \leq 1$$

It will be seen that (2.2) - (2.5) plus the appropriate one of (2.6) form a system of 8 algebraic and partial differential equations for the 8 evolutionary variables. Further details of the variable selection for computing their evolution are given in § 2.5

The model is posed for a rock matrix bed 90 metres wide (chosen as the x direction) by 60 metres deep (chosen as the z direction) with all properties and variables assumed to be constant in the horizontal y direction. The initial configuration is illustrated in Figure 2.1 showing that the bottom approximately two thirds are saturated with water ( $S_\ell = 1.0$ ) and the top third is at the residual unsaturated value ( $S_\ell = .1$ ) The boundary conditions are chosen so that the saturated zone resembles closely the fluid of the single phase saturated zone studies reviewed in § 1.2. I.e. the domain of the flow is an impermeable box with insulated sides. The temperature at the top of the layer is maintained at a constant  $= T_{\text{top}}$ , taken to be 20 °C in this study. and the temperature at the bottom of the layer is a parameter of the study and is varied between 70 °C and 150 °C. For a steady state bottom

temperature  $T_{\text{bot}}$ , in excess of 142 °C, a dynamic bottom temperature was used which decayed exponentially from 142 °C to  $T_{\text{bot}}$  with a time constant of 35 days, i.e.

$$\begin{aligned} T_{\text{bot}}(t) &= T_{\text{bot}} \quad \text{if } T_{\text{bot}} \leq 142^{\circ}\text{C} \\ &= T_{\text{bot}}(1 - w(t)) + 142w(t) \quad \text{if } T_{\text{bot}} > 142^{\circ}\text{C} \end{aligned}$$

for

$$w(t) = \exp(-t/35)$$

with  $t$  measured in days.

The choice of the cut-off temperature at 142 ° C and the time constant of 35 days in this dynamic boundary condition are pragmatic choices without particular physical significance. Basically, using the time step selection procedure described in § 2.6, the model was able to start without using excessively small time steps for bottom temperatures up to about 142 ° C, but beyond that the procedure selects increasingly small time steps, down to the size of hours, in its attempt to follow initial transient behaviour that is irrelevant to the desired steady state. The time constant of 35 days is much larger than these unduly small initial time steps, but small enough that the dynamic boundary condition has decayed away well before instability of interest in this study sets in.

The initial pressure field is essentially the hydrostatic one, with  $P = 100 \text{ Kpa}$  being the ‘air’ pressure in the unsaturated layer. Because the study uses the sealed box model of the single phase studies of the preceding subsection, the pressure field of the steady state solution is a consequence of the initial conditions and is not determined a priori. To reduce the influence of this, we have included a relatively large portion of the overlying unsaturated zone, and as a result the steady state pressure in this zone varies from 100 *Kpa* to 105 *Kpa* over the range of  $T_{\text{bot}}$  used.

A schematic glimpse of the steady state fluid field for bottom heating in the two phase convection regime is shown in Figure 2.2, in advance of the more detailed discussion of § 3. In this figure, two pockets of mixed phase fluid, primarily liquid water and steam, appear disrupting the horizontal separation of the vapour and liquid phases shown in Figure 2.1, that characterizes the flow regimes of lower bottom heating.

## 2.2 Discretization of the Model's Equations

Each of the three conservation laws equates the time rate of change of the density of a conserved quantity to the sum of divergences of fluxes of that quantity driven by gradients in some or all of phase potentials, gas phase mole fractions, or temperature. This form is reflected in a corresponding form for the discretized equations, which are formed by using standard conservative finite differencing based on square control volumes and totally implicit time discretization. A detailed description of the finite difference equations may be found in Forsyth,<sup>10</sup> 1990, but the general form can be explained as follows. We will use superscript "N" to denote the Nth time level of the discretization, and subscript "i" to denote the  $i^{\text{th}}$  mesh cell. We will use  $A_i^N$  to denote the amount of one of the three conserved quantities considered to be constant in cell  $i$  at time  $N$ , e.g., for the conservation of water,

$$A_i^N = \phi [S_\ell M_\ell X_w + S_g M_g Y_w]_i^N * \text{Vol}(i)$$

where  $\text{Vol}(i)$  is the volume of cell  $i$ . The discretized conservation laws, then, have the form

$$\begin{aligned} A_i^{N+1} - A_i^N - \Delta t \sum_{j \in \eta_i} \{ & Q_{ji}^{N+1}(A) (\psi_{\ell j}^{N+1} - \psi_{\ell i}^{N+1}) \\ & + R_{ji}^{N+1}(A) (\psi_{gj}^{N+1} - \psi_{gi}^{N+1}) \\ & + S_{ji}^{N+1}(A) (Y_{aj}^{N+1} - Y_{ai}^{N+1}) \\ & + U_{ji}^{N+1}(A) (Y_{wj}^{N+1} - Y_{wi}^{N+1}) \\ & + V_{ji}^{N+1}(A) (T_j^{N+1} - T_i^{N+1}) \} \\ & = 0 \end{aligned} \quad (2.7)$$

In (2.7),  $\eta_i$  is the set of four indices for the four neighbouring cells to cell  $i$ , and the terms in the summation represent the rate at which  $A$  flows from cell  $j$  into cell  $i$  as driven by the quantities differenced between cell  $j$  and cell  $i$ . We will refer to these summation terms as the discrete fluxes of  $A$ , e.g.  $Q_{ji}^{N+1}(A) (\psi_{\ell j}^{N+1} - \psi_{\ell i}^{N+1})$  is the discrete flux of  $A$  from cell  $j$  to cell  $i$  due to the differences in liquid phase potential between these cells. The coefficients  $Q, R, S, U, V$ , when present, combine the nonlinearities of the transport coefficients involving the state variables in cells  $i$  and  $j$  with geometric factors from these cells. The designation "(A)" only indicates that the transport coefficient is associated with conserved quantity  $A$ ; it is not intended to indicate a direct functional dependence on  $A$  as a variable. The transport

coefficients in  $Q(A)$  and  $R(A)$  are upstream weighted with the upstream direction determined by the liquid and gas phase potentials respectively. For the other coefficients, harmonic averaging is used. Not all of these coefficients are present in each discrete equation, e.g., for the conservation of water  $S_{ij}^{N+1}(A) = 0$  and  $V_{ji}^{N+1}(A) = 0$ .

### § 2.3 Solving the Implicit Equations

For the time stepping process, we assume that the 8 model variables are known for each cell at the  $N$ th time level, and that we have a provisional time step,  $\Delta t$ , to the next time level. If the time step yields a convergent iteration (see § 2.6), we can compute the 8 variables at the  $(N+1)$ th time level by advancing three of the variables using the discrete conservation laws, and then computing the remaining five variables from algebraic equations in (2.5) and (2.6). The five latter variables are referred to as secondary variables and the other three as primary variables; pressure and temperature are always primary variables, but the third depends on the phase state as described in § 2.5 below. Computing the next provisional time step is also a part of each time step as discussed in § 2.6.

The running times of these simulations are crucially dependent on the solution strategy used for solving the nonlinear equations of the discretized conservation laws. These strategies usually involve selecting a linearization technique (outer iteration) and a method for solving the resulting linear equations. Our strategy has been to use full Newton's method for the outer iteration with the incomplete factorization preconditioning plus the ORTHOMIN acceleration version of the preconditioned conjugate residual iteration for the linear equations, (Behie and Forsyth,<sup>2</sup> 1984, and Kightley and Forsyth,<sup>13</sup> 1989). The reliability of convergence, and enhanced time step size, provided by Newton's method, plus the efficiency of ORTHOMIN make this combination attractive.

Crucial to our use of full Newton's method is the capability of efficient numerical differentiation for approximating the Jacobian matrix of the nonlinear system. For the complex exact expressions and empirical dependencies of the nonlinear transport coefficients and thermodynamic relationships in this multiphase model, the manual evaluation of the analytic derivatives for the Jacobian matrix is a large and error prone task. The numerical evaluation of the resulting analytic expressions is expensive in computing time, and gives rise to complicated programming expressions, which are disincentives to change, or experiment with, the physical model. We have found that numerical differentiation produces effective approximations to the Jacobian matrix for Newton's method, with code that only evaluates the terms in

the equations themselves, not the derivatives. This enables us to use a full physical model at little additional effort.

In our monitoring of the performance of this strategy, we found that the time required for constructing the linear equations and the time required to solve them was roughly equal.

### § 2.4 Efficient Computation of the Numerical Jacobian

The special form of the discrete conservation laws permits an elementary reduction in the amount of computation necessary to form their Jacobian numerically. The basic principle of this reduction can be explained with less technical and notational complication if we illustrate the technique for the case of a single primary variable and a single conservation law.

Let  $u_i$  stand for the value of the primary variable in cell  $i$ , and let  $u$  denote the  $M$  vector of primary variables for  $M$  cells. Let  $A_i(u)$  be the amount of the conserved quantity in cell  $i$ ; and let  $f_{ji}(u)$ , for  $j \in \eta_i$ , be the discrete flux of  $A$  from cell  $j$  into cell  $i$ .

We assume that  $A_i(u)$  only depends on  $u_i$ ; we assume that  $f_{ji}(u)$  only depends on  $u_i$  and  $u_j$ , and this dependence is such that

$$f_{ji}(u) = -f_{ij}(u) \quad (2.8)$$

These assumptions are met by the finite differences used to construct the discrete form (2.7) of the conservation laws (2.2) - (2.4). Our example conservation law leads us to seek the solution,  $u$ , of a system of  $M$  equations of the form

$$g(u) = 0 \quad (2.9)$$

where

$$g_i(u) = A_i(u) - A_i(u^N) - \Delta t \sum_{j \in \eta_i} f_{ji}(u) \quad i = 1, M \quad (2.10)$$

and  $u^N$  is the  $M$  vector of known primary variable values at the current time,  $t_N$ . To solve (2.9) by Newton's method, we require the Jacobian matrix,  $J$ , for  $g$  i.e.,

$$J_{ik}(u) = \partial g_i(u) / \partial u_k \quad 1 \leq i \leq M; 1 \leq k \leq M. \quad (2.11)$$

For Newton's method, the  $(n+1)^{\text{st}}$  iterate,  $u^{(n+1)}$  is computed from the current iterate,  $u^{(n)}$ , by solving the correction equation



$$J(u^{(n)})c = -g(u^{(n)}) \quad (2.12)$$

and setting

$$u^{(n+1)} = u^{(n)} + c \quad (2.13)$$

To numerically approximate the entries of  $J$ , we use differencing interval  $\beta$ , in the  $k^{\text{th}}$  coordinate direction,  $e_k$ , i.e.,  $\beta$  is a scalar and  $e_k$  is the unit  $M$  vector with all components zero, except the  $k$ th. i.e.

$$e_{ki} = 0 \quad 1 \leq i \leq M, \quad i \neq k; \quad e_{kk} = 1. \quad (2.14)$$

Then

$$\partial g_i(u) / \partial u_k \approx \delta_k(\beta) A_i(u) - \Delta t \sum_{j \in \eta_i} \delta_k(\beta) f_{ji}(u) \quad (2.15)$$

for

$$\delta_k(\beta) A_i(u) = (A_i(u + \beta e_k) - A_i(u)) / \beta$$

$$\delta_k(\beta) f_{ji}(u) = (f_{ji}(u + \beta e_k) - f_{ji}(u)) / \beta$$

The entries in the  $k$ th column of  $J$  are  $\partial g_i(u) / \partial u_k$  for  $i = 1$  to  $M$  and we use the approximate values on the right side of (2.15) for them.

Now,

$$\delta_k A_i(u) = 0 \quad \text{unless } i = k \quad (2.16)$$

and

$$\delta_k f_{ji}(u) = 0 \quad \text{unless } i = k \text{ or } j = k \text{ and } j \in \eta_i. \quad (2.17)$$

If  $i = k$  then the diagonal entry of  $J$  is

$$\frac{\partial g_k}{\partial u_k}(u) \approx \delta_k(\beta) A_k(u_k) - \frac{\Delta t}{\beta} \sum_{j \in \eta_k} (f_{jk}(u + \beta e_k) - f_{jk}(u)) \quad (2.18)$$

If  $j = k$  and  $j \in \eta_i$ , then there is an off diagonal entry in the  $i$ th row and  $k$ th column of  $J$

$$\begin{aligned} \frac{\partial g_i}{\partial u_k}(u) &\approx -\frac{\Delta t}{\beta} (f_{ki}(u + \beta e_k) - f_{ki}(u)) \\ &= \frac{\Delta t}{\beta} (-f_{ik}(u + \beta e_k) + f_{ik}(u)) \end{aligned} \quad (2.19)$$

Note, however, that the two discrete flux values in the right hand approximate expression for  $\partial g_i(u)/\partial u_k$  in (2.19) have already appeared as summands in the summation  $j \in \eta_k$  in the approximate expression for  $\partial g_k(u)/\partial u_k$  in (2.18). If the evaluation of  $g_k(u+\beta e_k)$ ,  $k=1$  to  $M$  in (2.10) is regarded as  $M$  function evaluations, then it follows that the entire numerical Jacobian can be constructed in  $2M$  function evaluations. (This is independent of the number of dimensions!) Note that even if analytic derivatives are used,  $M$  function evaluations are required to calculate the residual for Newton's iteration. In the case of  $P$  primary variables and  $P$  conservations laws, this technique requires only  $(P+1)M$  function evaluations per Newton iteration.

### § 2.5 Changes of Phase, of Primary Variables, and Newton's Method

As indicated in § 2.3 , two of the primary variables for each mesh cell are the pressure,  $P$ , and the temperature,  $T$ , but the third depends on the phase state of the cell as per (2.6a-c). For a cell in the liquid saturated state,  $X_a$  is used as the third primary variable, and for a cell in the mixed phase state,  $S_\ell$  is used (Rubin and Buchanan, 1983).<sup>21</sup>

From each Newton iteration, a new set of values for the primary variables in each cell is computed. These may, however, not be physically permissible values, since they may violate the inequality constraints required in (2.6) for that state. It is the role of these constraints to signal changes of phase, and corresponding changes of primary variables. Figure 2.2 shows these transitions for the two states that occur in these computations\* .

For the switch from the liquid saturated state to the mixed state  $Y_a$  is reset to  $1 - Y_w$  , and in the reverse switch  $S_\ell$  is reset to 1.

The effect of a switch of primary variables is to change the system of equations to which Newton's method is being applied. This can happen repeatedly in the iterations for taking one time step, particularly when the pressure and temperature fields are causing dynamic changes of phase. In this circumstance, we do not attain the rapid, quadratic convergence of Newton's method; indeed, the time step must often be reduced to get convergence at all. An obvious alternative switching

---

\* If the cell were in the gas saturated state ( $S_\ell = 0$ ), then  $Y_a$  would be selected as the third primary variable ; however, in the computations reported here, this state does not occur.

strategy is to defer the switch until after a time step is completed. However, because a large number of cells may switch in a given timestep, this strategy seems to perform poorly compared to allowing switches after every Newton iteration. Deferring the switch until the end of a time step can result in a large number of cells which are in thermodynamically inconsistent states, which can result in a highly unstable situation requiring very small time steps. (See, however, Trangenstein and Bell,<sup>26</sup> 1989).

The change of phase state of a cell from liquid saturated ( $S_\ell = 1$ ) to mixed ( $0 < S_\ell < 1$ ) can happen in several ways. The liquid phase fluxes of the discrete versions of (2.2) - (2.4) may result in a net exit of the liquid into neighbouring cells leaving a previously saturated cell, unsaturated. E.g. If a saturated cell is above an unsaturated cell, with respect to gravity, the liquid will seep from the upper cell to the lower, (unless there is some overriding counter flux). Alternatively, the temperature in a cell may rise to the saturation temperature for the liquid at the pressure in the cell, so that some of the liquid is evaporated into the gaseous phase. As indicated in the previous subsection, computationally this can be recognized when the temperature and pressure in a liquid saturated cell result in  $Y_a + Y_w > 1$ , which is equivalent to

$$Z_a X_a + Z_w X_w > 1. \quad (2.20)$$

where  $Z_a, Z_w$  are the equilibrium ratios defined in Appendix A.

In the flows of our computations,  $X_a$  is very small, so that to a good approximation,  $X_w = 1$  and the saturation temperature, pressure relation reflected in (2.20) can be approximated by  $Z_w = 1$ . Our discussion is complicated by the fact that two conventional, but different, uses for the term ‘saturation’ are required - ‘saturation’ in the porous medium sense, and ‘saturation’ referring to the pressure temperature condition at which water evaporates. In hopes of reducing possible confusion, we will refer to the temperature above which, at a given pressure, water exists in both vapour and liquid phases as the bubble temperature (for the given pressure) and we will designate it  $T_{\text{bub}}$ . From  $Z_w = 1$  using the formula for  $Z_w$  of Appendix A, we conclude that

$$T_{\text{bub}} = -30.0 + (P \times 10^8 / .877)^{1/4.76} \text{ } ^\circ\text{C} . \quad (2.21)$$

At this temperature, increases in energy in the cell are diverted from raising the temperature of the liquid, (increasing its internal energy), to changing its phase, i.e., contributing to the gas phase internal energy in the form of the latent heat of

evaporation. Hence the temperature is ‘capped’ at  $T_{\text{bub}}$ , with regard to further injections of energy, at least until some of the assumptions of (2.21) are violated. This effect will be seen in the temperature distributions of the two phase convective flow regime of § 3.

## 2.6 Time Step Size Selection

The time stepping procedure can be viewed as attempting to take a time step with a provisional time step, using Newton’s method to solve the implicit equations. If Newton’s method converges, the provisional time step is accepted and the time variable and solution are updated appropriately. If Newton’s iteration fails to converge, the provisional time step is rejected. In either case, a new provisional time step is required, which is computed from the previous Newton’s iteration results, either to repeat the attempt at the current time level, or to attempt a step at the newly advanced time level.

The calculation of the new provisional step size is controlled by a fairly complicated set of parameters. For each variable, two parameters are used; the target change parameter, which specifies the desired change in the associated variable per time step, and the convergence tolerance parameter, which is the criterion for convergence of the Newton iteration for the associated variable. A further parameter is the maximum number of iterations allowed, i.e. the Newton iteration is deemed to have converged if the convergence criterion for each variable is met in the specified maximum number of iterations.

If the iteration does not converge, the new provisional step size is a reduction (typically, half) of the current rejected step size. If the Newton iteration converges, then, for each variable, the ratio of the target change parameter to the Newton correction in that variable is computed. The minimum of these ratios is used to multiply the current accepted step size to give the new provisional step size. The intention then is to control the step size so that the Newton corrections hit, or are less than, the target change parameters. An analysis of the error control implications of this kind of strategy is given in Eriksson and Johnson,<sup>9</sup> 1987.

### 3. Flow Regimes

For each value of  $T_{\text{bot}}$ , the flow develops from the common initial state described in the previous section into a dynamic flow/energy transport pattern, and ultimately settles into a steady state that is characteristic of  $T_{\text{bot}}$ . We can identify three basic flow regimes for these flow evolutions:

- i) the conduction regime - in which the dominant heat transfer mechanism is conduction through the liquid phase and rock matrix, and the fluid properties vary only with the depth coordinate  $z$
  
- (ii) the single phase convection regime - in which convection cells form in the liquid of the saturated zone, and provide significant heat transfer
  
- (iii) the two phase convection regime - in which two phase zones of water in the liquid and gaseous phases appear in the saturated layer's convection cells.

Details of these regimes are discussed in the subsections of this section, but we can summarize their relationships as follows. The model is initiated in the conductive regime. If  $T_{\text{bot}}$  is sufficiently small, the flow remains in this regime throughout its evolution: the fluid properties depending only on the depth coordinate  $z$ , and relaxing monotonically to their equilibrium values. For larger values of  $T_{\text{bot}}$ , the conductive regime is unstable, and the flow develops variations in the  $x$  coordinate direction, which evolve into convection cells. This instability develops earlier and is more pronounced as  $T_{\text{bot}}$  is increased. As long as the temperatures in the liquid saturated zone do not exceed the bubble temperature, as discussed in § 2.5, the flow remains in this second flow regime, and exhibits the basic phenomena of the single saturated liquid phase models reviewed in § 1.2.

For higher values of  $T_{\text{bot}}$  the flow starts in the unstable conductive regime, and soon starts evolving into the single phase convection regime. But before the convection cells are fully developed, the temperature in the hotter portions of the flow exceeds the local bubble temperature, and a two phase zone is initiated. In this zone, the temperature holds at the bubble temperature, limiting the development of the convection cell. These two phase zones expand and settle into a steady state, coexisting with the liquid phase convection cells, and forming partial heat pipes. They are characteristic of the third flow regime, which is not exhibited by the

simpler single phase models.

If the heat flux (in units of Joules/(m<sup>2</sup>-day)) is integrated in the x direction across the bottom of the (2 dimensional) box, we obtain a global heat transfer rate,  $Q_{\text{bot}}(t)$  (in units of Joules/(m-day)) that characterizes the rate of uptake of heat at time  $t$  by the bed from its isothermal base, per meter in the y direction (the horizontal direction in which the properties are all assumed uniform.) Similarly, integrating the heat flux across the top of the box, we obtain the heat transfer rate,  $Q_{\text{top}}(t)$ , that characterizes the rate of delivery of heat, at time  $t$ , by the bed to its isothermal top.

If the dynamic state of the box approaches a steady state as  $t \rightarrow \infty$ , then both  $Q_{\text{bot}}(t)$  and  $Q_{\text{top}}(t)$  approach the steady state heat transfer rate,  $\bar{Q}(T_{\text{bot}})$ , which we designate as depending on the parameter of our study,  $T_{\text{bot}}$ . Four histories of  $Q_{\text{bot}}(t)$  and  $Q_{\text{top}}(t)$  are shown in Figure 3.1 for  $T_{\text{bot}} = 80, 100, 120, \text{ and } 140$ . For each value of  $T_{\text{bot}}$ ,  $Q_{\text{bot}}(t)$  is the upper solid curve, and  $Q_{\text{top}}(t)$  is the lower dashed curve. As  $t$  approaches 200 years the upper and lower curves approach each other at a limiting value that define  $\bar{Q}(T_{\text{bot}})$  for each case. In Figure 4.2, a graph of  $\bar{Q}(T_{\text{bot}})$  versus  $T_{\text{bot}}$  is given.

There is, of course, a basic difficulty in identifying whether or not a numerical computation of dynamic behaviour has converged to a steady state. In this study, we have used inspection of these profiles to make this identification.

In the studies reviewed in § 1.2 of convection in a saturated zone, the Rayleigh number is used as a basic parameter of study that summarizes the relative importance of buoyancy forces to viscous forces in the fluid. When two phases of the fluid are present in the model, The Rayleigh number is less useful in characterizing the fluid since the buoyancies and viscosities of the liquid and vapour phases of the liquid are significantly different, and the transport is strongly affected by the phase change between them. Moreover, the Rayleigh number does not characterize the fluid, specifically the fraction of the fluid that is in the vapour phase, since the Rayleigh number depends on the temperature difference across the layer, but the vapour fraction depends on the absolute temperature, and the pressure, locally. A less fundamental difficulty with using the Rayleigh number to characterize the saturated zone alone, in the liquid convection regime of our study, is that the upper boundary of the liquid saturated zone does not have a constant temperature, unlike the studies of saturated zone convection in § 1.2.

For these reasons, we have not tried to use a Rayleigh number as a basic parameter of the study, but selected the bottom temperature for this purpose. To facilitate comparisons, however, a further discussion of Rayleigh number and the numerical values of the combined physical and geometric data that bear on it for our study are provided in Appendix B.

### 3.1 Formation of Convection Cells

For the three higher values of  $T_{\text{bot}}$ , the profiles of  $Q_{\text{bot}}(t)$ , in Figure 3.1 each show a pulse that is earlier, and steeper, with increasing  $T_{\text{bot}}$ . If we examine the temperature distributions during these episodes, we can see that the pulses are associated with the formation of convection cells. Figure 3.2-3.5 show the temperature distributions for  $T_{\text{bot}}=120^{\circ}\text{C}$ , for times 30, 42, 57, and 200 years. Figure 3.2 shows the temperature essentially independent of  $x$ , and the heat is being transferred essentially by conduction. However, the initiation of two ‘peaks’ and two ‘valleys’ in the lower portion of the bed is apparent in the temperature distribution at 42 years in Figure 3.3 and is highly developed by 57 years, as shown in Figure 3.4. These peaks of the temperature profile correspond to regions where the hot liquid water is rising from the bottom of the box, and the valleys correspond to regions where the water cooled near the interface with the unsaturated zone is sinking. The peaks and valleys of the temperature profiles internal to the flow field each mark the vertical boundary between two adjacent convection cells of opposite circulation pattern. Since the vertical walls of the box are impermeable, the boundaries at  $x=0$  and  $x=90$  m each form the boundary of a convection cell. In Figures 3.4 (and 3.5), it can be seen that three cells are present; the boundary at  $x=0$  is a region of upwelling of heated water, and the boundary at  $x=90$  m is a region of sinking of water cooled in the upper region near the surface of the saturated zone. This can be contrasted with the temperature profile of Figure 3.10(a) for  $T_{\text{bot}}=150^{\circ}\text{C}$ . Although the profile is clearly influenced by the vapour phase, two interior peaks are clearly present, indicating four convection cells, with cooler water sinking at both boundaries of the box.

Figure 3.5 shows the steady state temperature profile. Comparison with Figure 3.4 (the 57 year profile) shows that the temperature valleys of the steady state are higher, as are the peaks, i.e. the temperatures in the convection cells are higher. This difference reflects the convection cell formation mechanisms that explain the pulse in  $Q_{\text{bot}}(t)$  and the subsequent rise in  $Q_{\text{top}}(t)$  that appear in Figure 3.1. The

comparison of these temperature profiles can be made in more detail by inspecting the contour plot of Figure 3.6. In this plot, the dashed contours show the temperatures at 57 years and the solid curves show the temperatures at 200 years. The temperatures at 57 years, which is approximately the peak of the pulse, are lower than the steady state temperatures in the cooler regions of sinking liquid, resulting in stronger temperature gradients at the bottom of the layer (e.g. compare the  $90^{\circ}\text{C}$  contour in both cases.) This results in larger heat transfer rates through and near the bottom of the layer, resulting in large  $Q_{\text{top}}(t)$ . At this stage, the convection has not yet warmed the upper section of the saturated zone, and the dashed contours are lower than their solid counterparts of the steady state profile. Hence  $Q_{\text{top}}(t)$  remains relatively low. The convection subsequently warms the upper parts of the saturated zone pushing a major portion of the temperature gradient into the overlying unsaturated zone. In these latter stages, the water is less cooled in the upper regions of the saturated zone, and sinks less vigorously. The temperature contours in the lower part of the layer gradually space apart, reducing  $Q_{\text{bot}}(t)$  but crowd closer together in the unsaturated zone at the top of the layer, raising  $Q_{\text{top}}(t)$  until equilibrium is attained. These mechanisms are reflected in the decreasing and increasing segments of the profiles of  $Q_{\text{bot}}(t)$  and  $Q_{\text{top}}(t)$  respectively, for  $t > 60$  years, in Figure 3.1.

### 3.2 The Conduction Regime

Unlike the three profiles for  $Q_{\text{bot}}(t)$  and  $Q_{\text{top}}(t)$ , for  $T_{\text{bot}}=100, 200$  and  $140^{\circ}\text{C}$ , the profiles of these heat transfer rates for  $T_{\text{bot}}=80^{\circ}\text{C}$  in Figure 3.1 show no pulse in  $0 \leq t \leq 200$  years, but monotonically drop, and rise, respectively to their limiting value. There is, of course, no guarantee that a pulse marking the formation of convection cells does not occur for  $t > 200$  years. Indeed, the temperature distribution for  $T_{\text{bot}}=80^{\circ}\text{C}$  at constant depth shows a small, but regular variation with  $x$  - with a maximum total variation of  $.5^{\circ}\text{C}$  on the line of depth 40 meters. Hence it seems likely that weak convection cells are present, or forming. Nevertheless, this effect is so small that it seems appropriate to classify this flow as being in the conduction regime, for heat transfer purposes. The same is true for  $T_{\text{bot}}=85^{\circ}\text{C}$ , however, for  $T_{\text{bot}}=90^{\circ}\text{C}$ , a weak but clearly defined pulse appears in the profile of  $Q_{\text{bot}}(t)$ , which starts its rise at  $t=110$  years and peaks at 180 years. The corresponding temperature distribution shows a single internal peak temperature i.e. a pair of convection cells formed.



Integration of the dynamic equations is an inefficient way to determine the bifurcation characteristics of the steady state, and it is not clear from these calculations whether there is a critical value of  $T_{\text{bot}}$  (crit) such that purely conduction solutions exist for the steady state version of this model when  $T_{\text{bot}} < T_{\text{bot}}(\text{crit})$ , but convection cells exist for  $T_{\text{bot}} > T_{\text{bot}}(\text{crit})$ . Bifurcation and path continuation techniques as discussed in Glowinski, Keller, and Rheinart<sup>11</sup>, 1985, and Seydel<sup>24</sup>, 1988, are designed for this purpose. We can however, compute Rayleigh numbers for the single phase (liquid saturated) layer for  $T_{\text{bot}}=80$  and  $85$ , which are bottom temperatures close to that at which convection cells become computationally significant, since the temperature is essentially constant at the surface of the saturated zone. These Rayleigh numbers can then be compared to the critical Rayleigh numbers of the single phase models reviewed in § 1.2. The single phase layer is 37 meters wide and has upper temperatures of 44.1 and 48.0 for  $T_{\text{bot}}=80$  and  $85$ , respectively. Based on the definition of Rayleigh number given in Appendix B, the corresponding Rayleigh numbers are 18 and 18.5 respectively. If the critical Rayleigh number is reviewed as an approximate indicator of when convection effects start to become significant, then these values can be viewed as being reasonably consistent with the values obtained by Nield<sup>17</sup>, 1968 discussed in § 1.2, which lie in the range 9 to 27 for the simpler single phase model and various boundary conditions that could be applied to this layer.

### 3.3 Appearance of the Vapour Phase

The vapour phase appears in the flow locally where the temperature exceeds the liquid bubble temperature,  $T_{\text{bub}}$ , (i.e. the ‘boiling’ point,) which has been discussed in § 2.6. and is repeated here in (3.1)

$$T_{\text{bub}}(P) = -30. + (P \times 10^8 / .877)^{1/4.76} \text{ } ^\circ\text{C} . \quad (3.1)$$

The primary variation in pressure is the hydrostatic variation with depth. Hence  $T_{\text{bub}}$  is significantly depth dependent. In our modeling, the liquid saturation zone starts at a depth of 23 meters. The pressure in the overlying unsaturated zone, which we denote by  $P_0$ , is slightly variable due to the sealed box conditions, varying from 101 Kpa to 105 Kpa. Consequently, the hydrostatic pressure in Kpa is

$$P_H(z) = \rho_l g(-z - 23) + P_0 \text{ for } z < -23. \quad (3.2)$$

For  $P_0=100$ , the variation of the bubble temperature with depth due to the hydrostatic pressure profile of (3.2) is given in Table 3.1:

Figures 3.7-3.9 show several stages in the development of convection cells and two phase zones for  $T_{\text{bot}}=150^\circ\text{C}$ ; part (a) of each figure shows the temperature distribution and part (b) shows the liquid saturation,  $S_\ell$ . In Figures 3.7, the early emergence of convection cells can be seen. In this case, four cells are forming, showing two internal upwelling zones, or temperature peaks, that mark the common boundary of adjacent cells of opposing rotation. In this dynamically unstable evolution, the peaks are not identical, however, with the one in the foreground, at  $x=65$  m being hotter. The temperatures in the latter peak reach the local bubble temperature at depths of between 30 and 40 m and a two phase zone forms within the saturated liquid zone as can be seen in Figure 3.7 (b).

In Figures 3.8 for  $t=28.8$  years, the cells are more fully developed. The liquid saturation profile in Figure 3.8 (b) shows that the two phase zone which was initiated in Figures 3.7 has expanded and reached the surface of the saturated liquid zone, and the temperatures in the upwelling region centred on  $x=15$  m have reached the local bubble temperatures so that a second internal two phase zone has appeared. The larger two phase zone in Figure 3.8 (b) which has burst through the surface of the liquid saturated region shows a small region of condensation at its top, in the overlying unsaturated region. This zone is in the process of forming a heat pipe, evaporating the liquid in its lower, warmer, portion and condensing it at the cooler, higher portion. The temperature distribution in this two phase zone is being constrained by the bubble temperature. In its lower portion, the temperature peak is noticeably flattened, as the heat is being used to evaporate the liquid. At the upper portion, a small, flat ledge of higher temperatures can be seen in the condensing zone, where the latent heat of condensation is being released. This can also be seen in the contour plot of Figure 3.9, which shows the temperatures distribution at  $t=28.8$  years with solid curves, and the local bubble temperature with dashed contours. In the upwelling zone at  $x=65$  m., the constraining of the temperature to the local bubble temperature in the two phase zone is very clear. In the other upwelling zone at  $x=15$  m., it can be seen that the temperature contours for  $T=120$ , and 130 coincide with the local bubble temperature contours of the same values at depths of about 30 to 40 m., indicating the formation of the second two phase zone apparent in Figure 3.8 (b). However, in the rest of that region the temperature lies below the local bubble temperatures.

The distributions at 200 years are seen in Figure 3.10, considered to be the steady state distributions; the two upwelling regions are more closely equal. In each of them, a two phase convection zone has formed which evaporates the liquid in its lower portion in the liquid saturated zone, and condenses the vapour in its upper portion, in the unsaturated zone. The constraining of the temperature by  $T_{\text{bub}}$  in both of these zones is clear in Figure 3.10a, and the contour plot Figure 3.11, which shows the steady state temperatures as solid contours, and the local bubble temperatures as dashed contours.

The asymmetries of Figures 3.8 and 3.9 seem primarily due to the different rates at which the corresponding pairs of convection cells develop dynamically under these particular initial conditions, perturbations due to terminations of Newton's method, and round-off errors. Figures 3.10 and 3.11 also show minor asymmetries between the left and right pairs of convection cells, but these are not due to transient effects since the dynamic changes have essentially died away before 150 years, as shown in Figure 3.1. The usual mathematical argument for the symmetry of the equilibrium state does not apply here, since it requires the uniqueness of the solution which is not present in the instability phenomena for nonlinear equations. It is plausible then that there are two different solutions with four convection cells, of which we have computed one.

#### 4. Some Conclusions

The two phase, two component model appears to be a interesting computationally viable, extension of the single phase models for heat and fluid transport in a bottom heated layer of water in a porous medium. It reproduces the phenomena of the simpler model in the appropriate heating ranges, and incorporates the phase changes and corresponding alternative heat transport , for higher bottom heating. The heat transfer characteristics of the extended model's runs are described in section 4.2.

We have demonstrated that the two dimensional extended model on a relatively small mesh, using current numerical techniques , poses a computation that is within the scope of relatively common and inexpensive workstations. The cells of the mesh for solving the extended model's equations were 3 metres square; the mesh was 20 cells deep by 30 cells wide. Although several variations in cell size, and mesh configuration were checked, no appreciable variation in phenomena was observed, and the discretization errors are estimated to be about 5% or less. The running times for the simulations depended heavily on the flow regime. Using a SUN 3/160 with a WEITEK floating point accelerator (running at about .2 MFLOPS), simulations for the conduction regime took typically an hour, while simulations for the two phase convective zone took up to 20 hours. Significant further efficiencies could probably be realized by improvements in time step control, particularly in two phase flows. Because of the complexity of the automatic step size control algorithm for this model, particularly in the presence of changes of state, we interactively modified the time step size control parameters as described in the next subsection.

##### 4.1 Time step size selection

Since each time step involves substantial computations, the appropriate choice of time step size is an important efficiency consideration. This choice complicated however by the dependence of the appropriate time step size on the model's behaviour, i.e. on the current heat transfer regime. In Figure 4.1, a profile of step size variation for subsequent time steps is shown for  $T_{\text{bot}} = 150 \text{ }^\circ\text{C}$  for the step size strategy of section 2.7 In the initial portion of the profile while the solution is primarily in the conductive regime, the step size grows rapidly, if the target change parameters are large enough. As the convection cells start to form, and the flow enters the single phase convection regime, the appropriate step size drops to allow the numerical solution to follow the developing flow. At this stage, the most relevant target change parameter is associated with the temperature. If the target change

parameters are too high, i.e. are at values appropriate for the conductive regime, then an oscillation in the selected step size will occur, since the projected step size will invariably be too large for the convergence of Newton's iteration. Such oscillations are quite inefficient, since the nonconvergent computation with the larger step size is discarded.

If the flow now enters the two phase convection regime as a result of vaporizing in local 'hotspots' in the liquid convection cells, the appropriate step sizes are typically further reduced due to the degradation of Newton's iteration resulting from primary variable switching. The parameters associated with the saturation variable becomes more relevant and a further oscillation in step size selected is likely, unless the target change parameters are further reduced. As the steady state is approached in the two phase convection regime, an oscillation in step size is almost unavoidable, under this strategy. Small target change parameters admit large step sizes as the steady state is approached; however, a number of mesh cells are close to the bubble temperature, and for these cells, primary variable switching can occur at each Newton iteration, preventing convergence unless the step size is small enough.

Rather than attempt to develop adaptive algorithms for controlling the time step size selection parameters, we elected to implement a technique for monitoring the calculation and modifying these parameters appropriately for the current state of the solution. The technique involves two files for the executing program; the monitoring file and the current parameters file. The executing program writes details of each Newton's iteration in the monitoring file, which we can review to check the progress of the computation using the current parameter values. If we wish to change the current parameters, we first lock the executing program out from reading the current parameters file, change the parameter values with a text editor, and then unlock the access by the executing program. On the executing program side, immediately prior to computing a provisional time step as described above, the program determines whether it is locked out from reading the current parameters file. If it is not, then it reads their values in (which may or may not have been modified) and uses them to compute the provisional time step; if it is locked out, it uses the existing internal parameter values.

This techniques allows the executing program to run for long periods of time unattended, but for a user to modify the parameters at will. A third file, called a lockfile can be used to provide the locking/unlocking mechanism in a manner that conforms to the FORTRAN 77 standard. To lock the program, we create the lockfile (which may be empty) and to unlock it, we delete the lockfile. The program

issues an INQUIRE command to determine if the lockfile is present in the file directory. If it is present, then the program knows it is locked out of the current parameters file.

The timestep profiles shown in Figures 4.1 and 4.2 were obtained for  $T_{bot} = 150^\circ\text{C}$  using this monitoring parameter modifying technique. The sudden drop in the step size at step about 50 and 100 are due to decreases in the temperature target change parameter at those stages. The inefficient oscillation in the time step size at the end of the run is clearly in evidence. The program was simply left to run at that stage.

## 4.2 Heat Transfer Characteristics

Using the basic, dimensioned, parameters of this study, we can observe the heat transfer characteristics for this model in Figure 4.3, where the bottom temperature is plotted against the steady state heat transfer rate,  $\bar{Q}(T_{bot})$ , as defined in Section 3. In this plot, four values of  $T_{bot}$  have been used in each of the conduction regime ( $70^\circ\text{C} - 85^\circ\text{C}$ ) and five values in each of the single phase convection regime ( $90^\circ\text{C} - 120^\circ\text{C}$ ) and the two phase convection regime ( $130^\circ\text{C} - 150^\circ\text{C}$ ).

The well known role of convection in enhancing heat transfer in the single phase convection regime, as reviewed in section 1.2 and referenced literature is evident in Figure 4.3.

In the two phase convection regime, two new effects are encountered, which work counter to each other. Firstly, the phase change inhibits the effectiveness of the convection cells for heat transfer in the liquid phase by capping the temperature at  $T_{bub}$  and disrupting the flow pattern of the cell. On the other hand, the partial heat pipe that forms in the two phase zones enhances the heat transfer. It is not clear from Figure 4.3 which of these effects dominates; the heat transfer rate rises fairly sharply to  $145^\circ\text{C}$  and then appears to level off somewhat, which coincides with a change in steady state solution structure from three convection cells to four.

At higher bottom heating, a vapour layer forms at the lower boundary. While this is a very interesting phenomenon, we feel that the isothermal bottom model is inappropriate for its study, because the solution behaviour becomes very temperature sensitive as  $T_{bot}$  approaches  $T_{bub}$ . It seems to us that a constant heat flux lower boundary condition would be more suited to the study of vapor formation at the bottom of a heated bed.

## References

1. H H Bau and K E Torrance, "Boiling in Low-Permeability Porous Materials," *Int J Heat mass Transf*, **25** pp. 45-55 (1982).
2. G. A. Behie and P. A. Forsyth, "Incomplete Factorization Methods for Fully Implicit Simulation of Enhanced," *SIAM J. Sci. Stat. Comput.*, **5**(3) pp. 543-561 (1984).
3. B Borkowska-Pawlak and W Kordylewski, "Stability of Two-Dimensional Natural Convection in a Porous Layer," *Mech Appl Math*, **35** pp. 279-290 (1982).
4. J P Caltagirone, "Thermoconvective Instabilities in a Horizontal Porous Layer," *J Fluid Mech*, **72** pp. 269-287 (1975).
5. J P Caltagirone and S Bories, "Solutions and Stability Criteria of Natural Convective Flow in an Inclined Porous Layer," *J Fluid Mech*, **155** pp. 267-287 (1985).
6. P Cheng, "Heat Transfer in Geothermal Systems," *Advances in Heat Transfer*, **14** pp. 1-105 (1978).
7. M A Combarous and S A Bories, "Hydrothermal Convection in Saturated Porous Media," *Adv Hydroscience*, **10** pp. 231-307 (1975).
8. M R Davidson, "Natural convection of Gas/Vapour Mixtures in a Porous Medium," *Int J Heat Mass Transf*, **29** pp. 1371-1381 (1986).
9. K Eriksson and C Johnson, "Error Estimates and Automatic Time Step Control for Nonlinear Parabolic Problems, I," *SIAM J of Num Anal*, **24** pp. 12-23 (1987).
10. P A Forsyth, "Radioactive Waste Disposal Heating Effects in Unsaturated Fractured Rock," *Num Heat Trans*, **17** pp. 29-51 (1990).
11. R Glowinski, H B Keller, and L Reinhart, "Continuation-Conjugate Gradient Methods for the Least Squares Solution of Nonlinear Boundary Value Problems," *SIAM J. Sci. Stat. Comput.*, **6** pp. 793-832 (1985).
12. H C Hardee and R H Nilson, "Natural Convection in Porous Media with Heat Generation," *Nuclear Science and Engineering*, **63** pp. 119-132 (1977).
13. J R Kightley and P A Forsyth, *WATSIT Iterative Sparse Matrix Solver: User's Guide*, Department of Computer Science, University of Waterloo (Feb 1989).

14. S Kimura, G Schubert, and J M Straus, "Route to Chaos in Porous-Medium Thermal Convection," *J of Fluid Mech*, **166** pp. 305-324 (1986).
15. C H Lai, G S Bodvarsson, and P A Witherspoon, "Second-Order Upwind Differencing Method for Nonisothermal Chemical Transport in Porous Media," *Num Heat Trans.*, **9**(1986).
16. S L Moya, E Ramos, and M Sen, "Numerical Study of Natural Convection in a Tilted Rectangular Porous Material," *Intl J of Heat Mass Transf*, **30** pp. 741-756 (1987).
17. D A Nield, "Onset of Thermohaline Convection in a Porous Medium," *Water Resources Research*, **4** pp. 553-560 (1968).
18. D W Pollock, "Simulation of Fluid Flow and Energy Transport Processes Associated With High-Level Radioactive Waste Disposal in Unsaturated Alluvium," *Water Res. Resrch*, **22** pp. 765-775 (1986).
19. K Pruess, "Modeling of Geothermal Reservoirs: Fundamental Processes, Computer Simulation and Field Applications," *Geothermics*, **19** pp. 3-15 (1990).
20. Y F Rao, K Fukuda, and S Hasegawa, "A Numerical Study of Three-Dimensional Natural Convection in a Horizontal Porous Annulus with Galerkin Method," *Int J Heat Mass Trans*, **31** pp. 695-707 (1988).
21. B Rubin and W Buchanan, "A General Purpose Thermal Model," SPE California Regional Meeting ,, Society of Petroleum Engineering (1983).
22. G Schubert and J M Straus, "Gravitational Stability of Water Over Steam in Vapor-Dominated Geothermal Systems," *J of Geo Res*, **85** pp. 6505-6512 (1980).
23. M Sen, P Vasseur, and L Robillard, "Multiple Steady States for Unicellular Natural Convection in an Inclined Porous Layer," *Intl J Heat Mass Transf*, **30** pp. 2097-2113 (1987).
24. R Seydel, *From Equilibrium to Chaos - Practical Bifurcation and Stability Analysis*, Elsevier (1988).
25. C H Sondergeld and D L Turcotte, "A Experimental Study of Two-Phase Convection in a Porous Medium with Applications to Geological Problems," *J of Geophy Res*, **82** pp. 2045-2053 (1977).
26. J A Trangenstein and J B Bell, "Mathematical Structure of Compositional Reservoir Simulation," *SIAM J. Sci. Stat. Comput.*, **10** pp. 817-845 (1989).



27. Y W Tsang and K Pruess, "A Study of Thermally Induced Convection Near a High-Level Waste Repository in Partially Saturated Fractured Tuff," *Water Res Resrch*, **23** pp. 1958-1966 (1987).
28. K S Udell, "Heat Transfer in Porous Media Considering Phase Change and Capillarity - the Heat Pipe Effect," *Int J Heat Mass Transf*, **28** pp. 485-495 (1985).

## Appendix A

This Appendix gives values of parameters and the correlations used for various physical properties of the extended model. As in section 2 the following subscript associations are followed:

$w$  - water ;  $a$  - air ;  $R$  - rock

$\ell$  - liquid phase ;  $g$  - gas phase ;  $s$  - reference standard

Pressure

$$P \quad Kpa$$

Molar Densities

$$M_w = M_{ws} [1 + \alpha_w (P - P_s) - \beta_w (T - T_s)] \quad \text{mole} / m^3$$

$$M_{ws} = 5.55 \times 10^4 \quad \text{mole} / m^3$$

$$\alpha_w = 4.3 \times 10^{-6} \quad (Kpa)^{-1}$$

$$\beta_w = 2.5 \times 10^{-4} \quad (^\circ K)^{-1}$$

$$T_s = 273 \quad ^\circ K$$

$$P_s = 100 \quad Kpa$$

$$M_g = P / R T \quad \text{mole} / m^3$$

$$R = 8.314 \times 10^{-3} \quad Kpa - m^3 / (\text{mol} - ^\circ K)$$

Mass Density

$$\rho_\ell = M_w (W_w X_w + W_a X_a) \quad Kg / m^3$$

$$\rho_g = M_g (W_w Y_w + W_a Y_a) \quad Kg / m^3$$

$$W_w = 18.02 \times 10^{-3} \quad Kg / \text{mole}$$

$$W_a = 28.97 \times 10^{-3} \quad Kg / \text{mole}$$

Equilibrium ratios:

$$Y_a = Z_a X_a$$

$$Y_w = Z_w X_w$$

$$Z_a = 1 \times 10^9 / (7.6 P \alpha^*)$$

$\alpha^*$  linearly interpolated from Table A.1

$$Z_w = \frac{.8777 \times 10^{-8} (T - 243)^{4.76}}{P}$$

Enthalpies:

$$h_\ell = C_w (T - T_s) X_w + C_a (T - T_s) X_a \quad J / \text{mole}$$

$$C_w = 75.4 \quad J / (\text{mole} \cdot ^\circ K)$$

$$C_a = 29.2 \quad J / (\text{mole} \cdot ^\circ K)$$

$$T_s = 273^\circ K$$

$$h_{ga} = C_a (T - T_s) \quad J / \text{mole}$$

$$H_{gw} = C_w (T - T_s) + h_{\text{lat}} \quad J / \text{mole}$$

$$h_{\text{lat}} = 4.814 \times 10^3 (T_c - T)^{.38} \quad J / \text{mole } T < T_c$$

$$= 0 \quad T > T_c$$

$$T_c = 647.3 \quad ^\circ K$$

$$h_g = Y_w h_{hw} + Y_a h_{ga}$$

Internal Energies

$$U_w = h_w - \frac{P \times 10^3}{M_w} \quad J / \text{mole}$$

$$U_g = h_g - \frac{P \times 10^3}{M_g} \quad J / \text{mole}$$

Heat capacity of rock

$$U_R M_R = 2.35 \times 10^6 \quad J / (m^3 - ^\circ K)$$

Viscosities

$$\mu_{(l)} = 10^{-9} / (12.1 + 2.88 (T - T_s) + 7.78 \times 10^{-4} (T - T_s)^2) \quad Kpa \text{ -day}$$

$$\mu_g = 10^{-13} (1.574 + .0044 (T - T_s)) \quad Kpa \text{ -day}$$

Gas phase diffusivity<sup>1</sup>

$$D_g = \frac{D_g^0 \phi S_g (T / 273)^{2.334}}{(P / 100)}$$

Permeabilities

Absolute permeability  $K = 10^{-12} \quad m^2$ . The relative permeabilities in the unsaturated states are obtained by linear interpolation in Table A.2

Porosity

$$\phi = 0.4$$

Effective heat conductivity

$$\lambda_H = (1-\phi)\lambda_r + \phi S_l \lambda_w$$

$$\lambda_r = 7.0 \quad \times 10^4 \quad J / (m^3 - ^\circ K \text{ - day})$$

$$\lambda_w = 5.35 \quad \times 10^4 \quad J / (m^3 - ^\circ K \text{ - day})$$

Gravitational Acceleration

$$g = 9.8066 \quad m / \text{sec}^2$$

---

<sup>1</sup> Y. Tsang and K. Pruess, 'A study of Thermally Induced Convection Near a High Level Nuclear Waste Repository in Partially Saturated Fractured Tuff,' Water Res. Res. 23 (1983) 1958-1966

## Appendix B

In the introduction to § 3, an explanation is presented for why we feel the Rayleigh number is an inappropriate basic parameter for this study involving a fluid that is an evaporating two phase liquid. However, to help facilitate comparisons with other work, particularly for the liquid phase convection regime, we present the following derivation.

The Rayleigh number for a horizontal liquid saturated layer ( $S_\ell = 1$ ) is defined to be:

$$R_a = b \beta_w C_w g M_{ws} K (T_{\text{bot}} - T_{\text{top}}) / \nu \lambda_H .$$

In addition to the symbols given in Appendix A, this formula requires:

$b$  - liquid saturated layer thickness = 37.  $m$

$\nu$  - kinematic viscosity of water =  $10^{-6} \quad m^2 / \text{sec}$

$$\lambda_H = .7624 \quad J / (\text{°K} - m - \text{sec}) .$$

(repeated for  $S_\ell = 1$  , in units required for  $R_a$  ) .

Evaluation of  $R_a$  for the parameter values given here and in Appendix A results in

$$R_a = .5 (T_{\text{bot}} - T_{\text{top}}) .$$

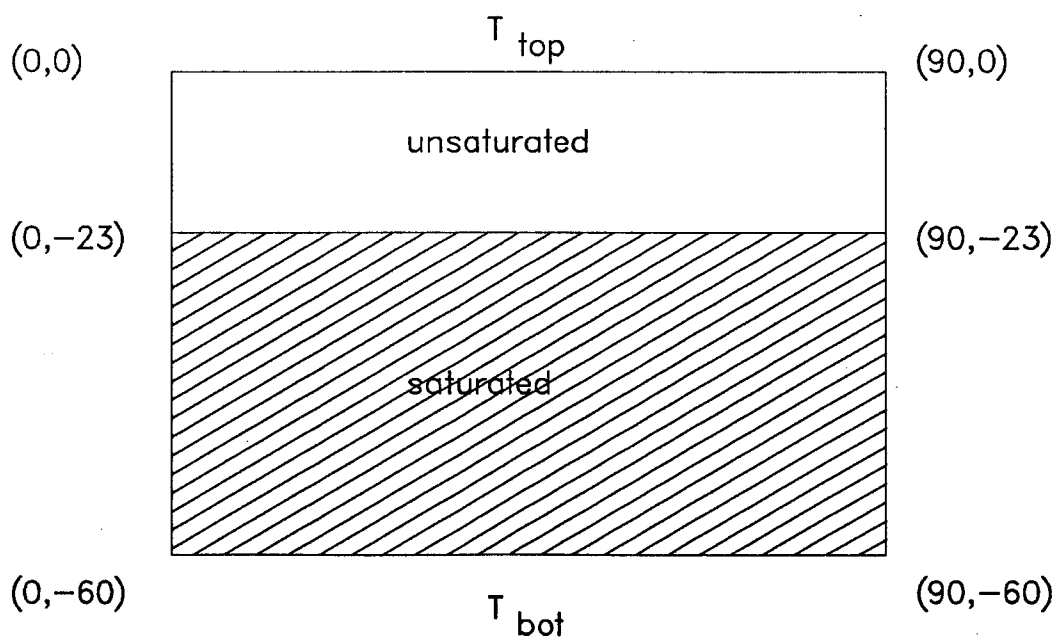
## List of Figures

- 2.1 Extended model geometry.
- 2.2 Schematic view of saturation zones.
- 2.3 Transition rules for phase change.
- 3.1 Heat transfer histories.
- 3.2 Temperature at 30 years, bottom temperature 120 ° C.
- 3.3 Temperature at 42 years, bottom temperature 120 ° C.
- 3.4 Temperature at 57 years, bottom temperature 120 ° C.
- 3.5 Temperature at 200 years, bottom temperature 120 ° C.
- 3.6 Temperature contours.
- 3.7(a) Temperature at 24.2 years, bottom temperature 150 ° C.
- 3.8(a) Temperature at 28.8 years, bottom temperature 150 ° C.
- 3.8(b) Water saturation at 28.8 years, bottom temperature 150 ° C.
- 3.9 Temperature contours, bottom temperature 150 ° C.
- 3.10(a) Temperature surface at 200 years, bottom temperature 150 ° C.
- 3.10(b) Water saturation at 200 years, bottom temperature 150 ° C.
- 3.11 Temperature contours at 200 years, bottom temperature 150 ° C.
- 4.1 Typical timestep size profile, for a two phase problem.
- 4.2 Timestep size profile as a function of absolute time.
- 4.3 Heat transfer characteristics.

## List of Tables

- 3.1 Variation of hydrostatic pressure and  $T_{byb}$  with depth.
- A.1 Parameter for computing  $Z_a$ .
- A.2 Unsaturated zone relative permeabilities.

Figure 2.1



Extended Model Geometry



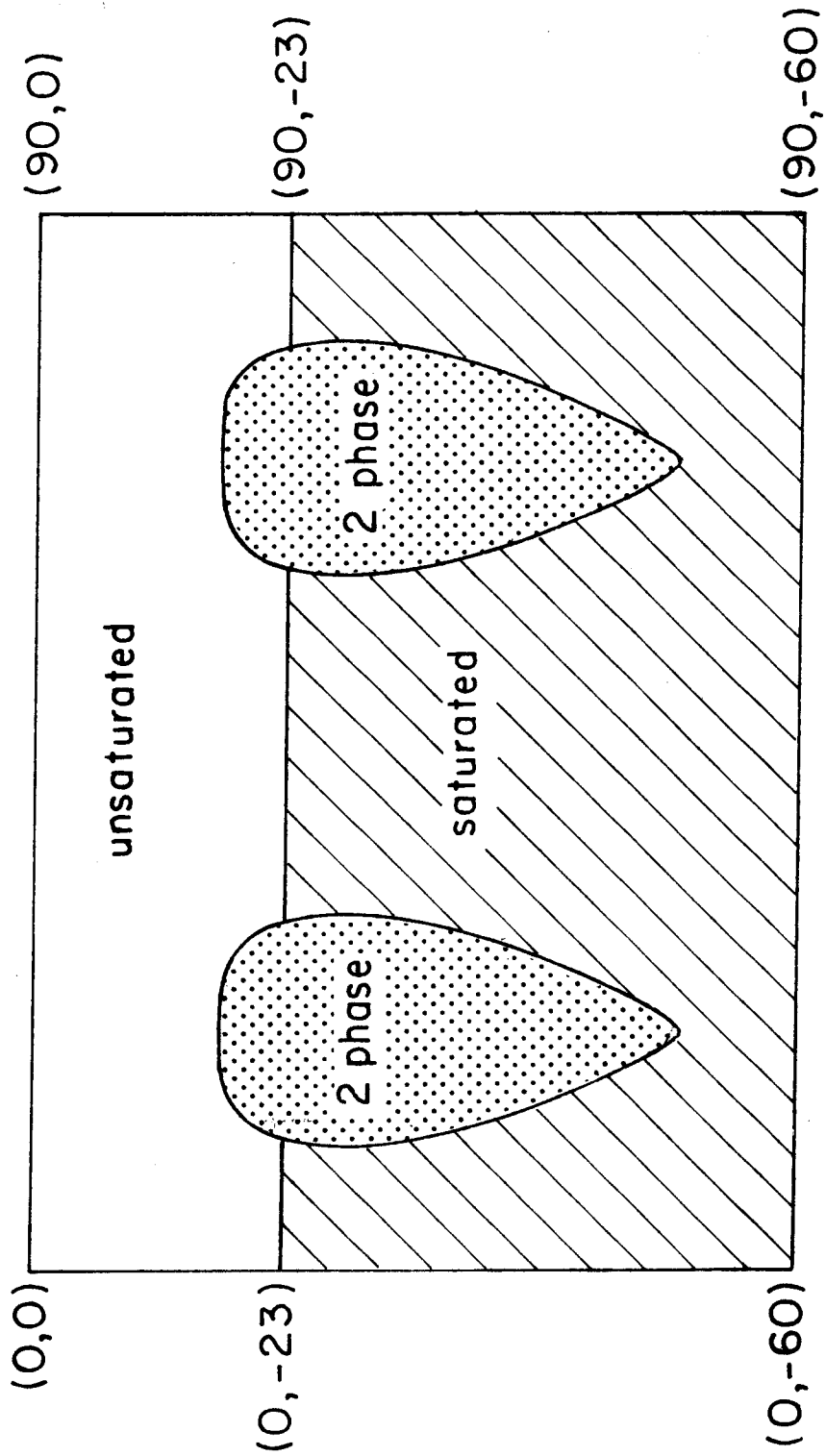


Figure 2.2

Schematic view of saturation zones for steady state, bottom temperature = 150° C ( See Figure 3.10 for quantitative details )

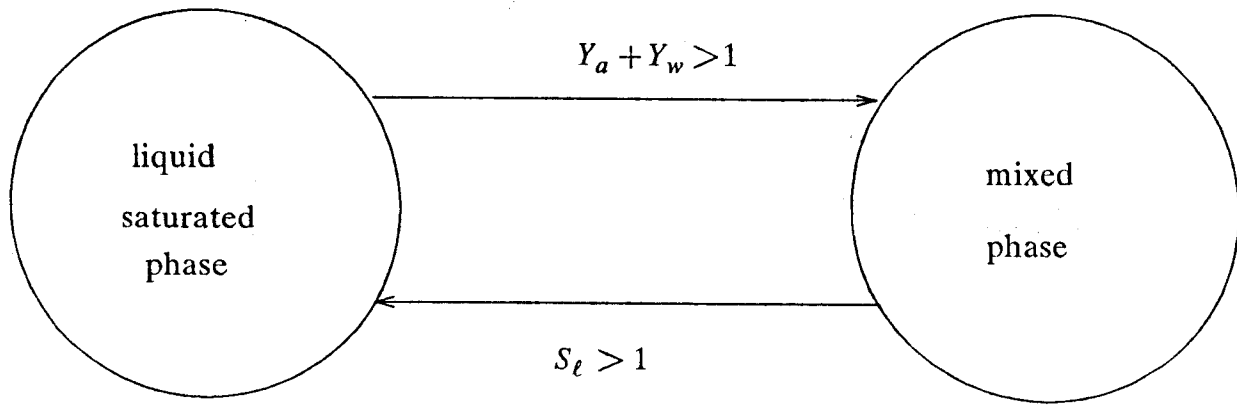
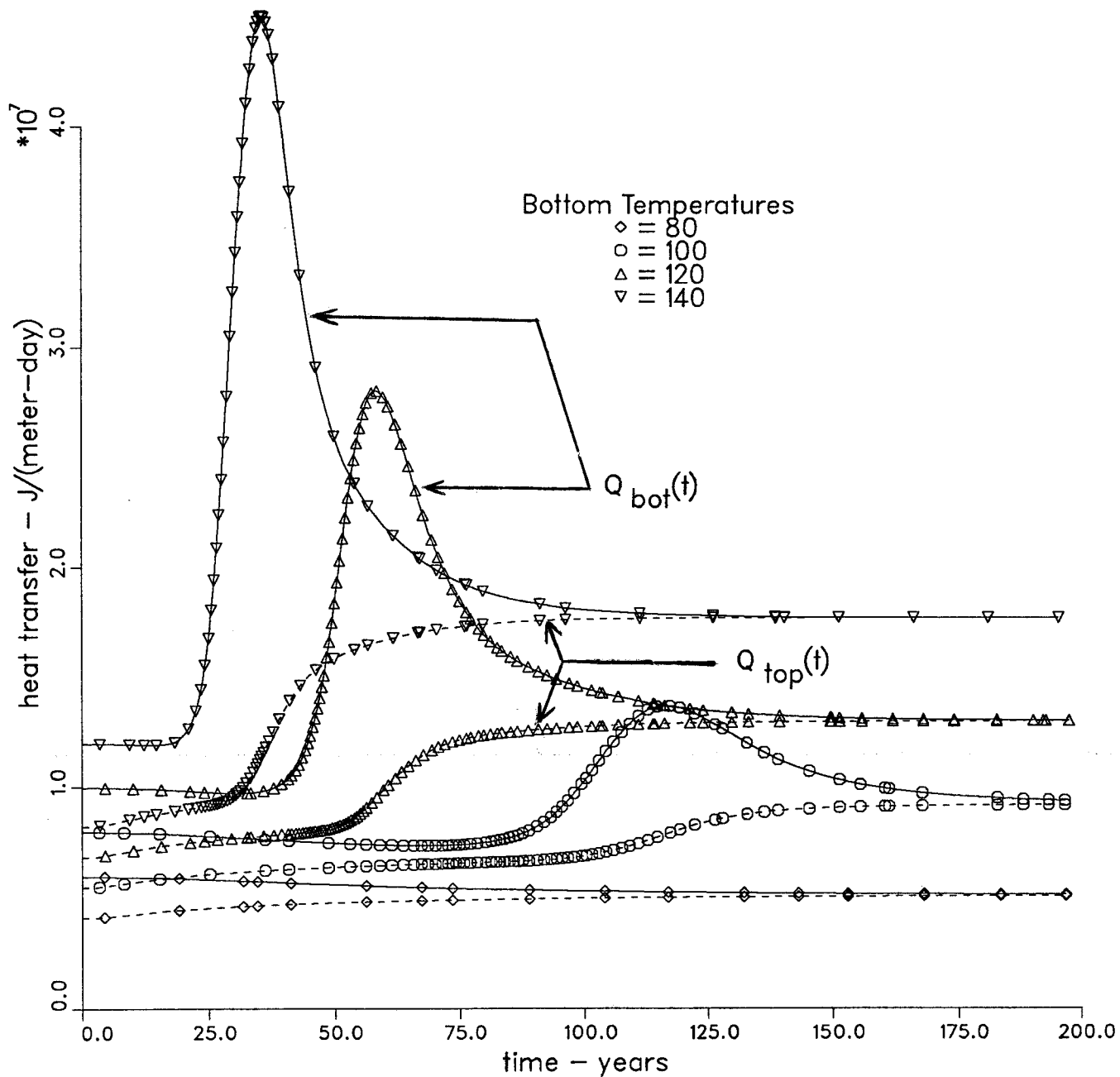


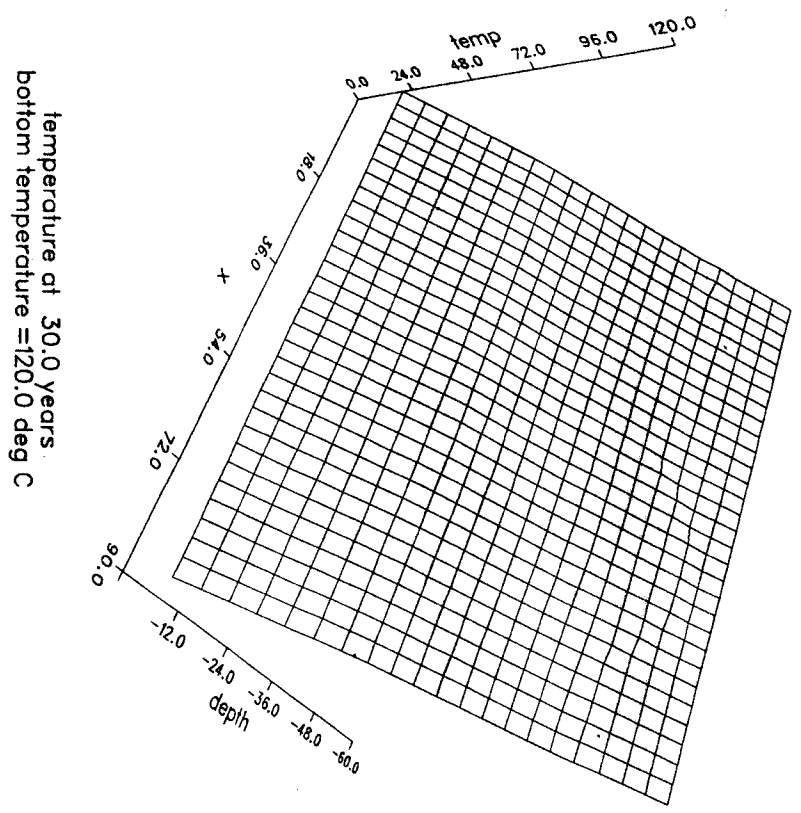
Figure 2.3  
Phase Transition Diagram

Figure 3.1



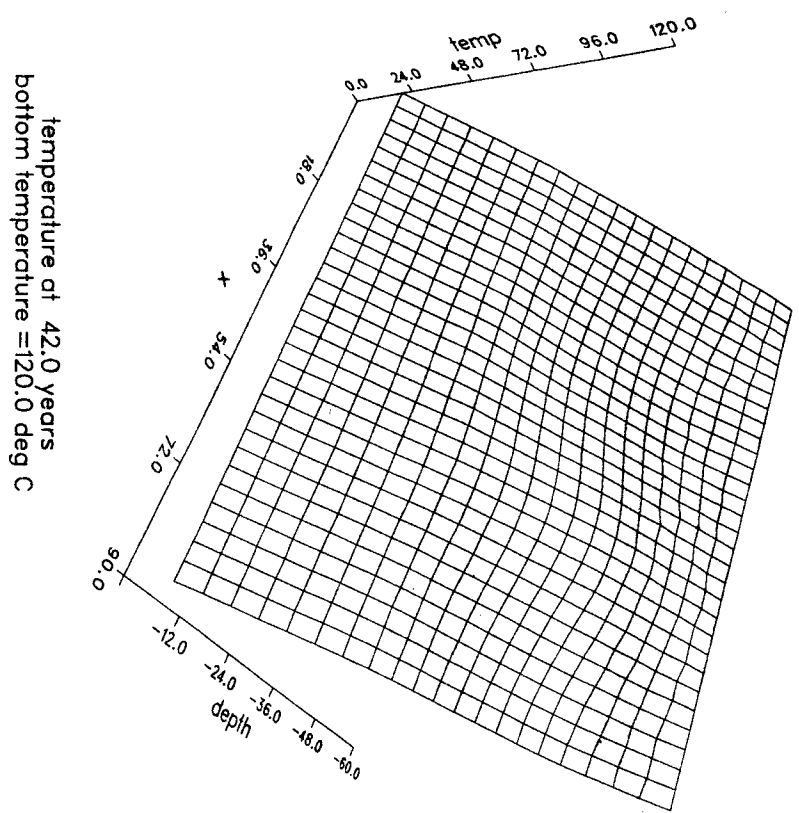
Heat Transfer Histories

Figure 3.2



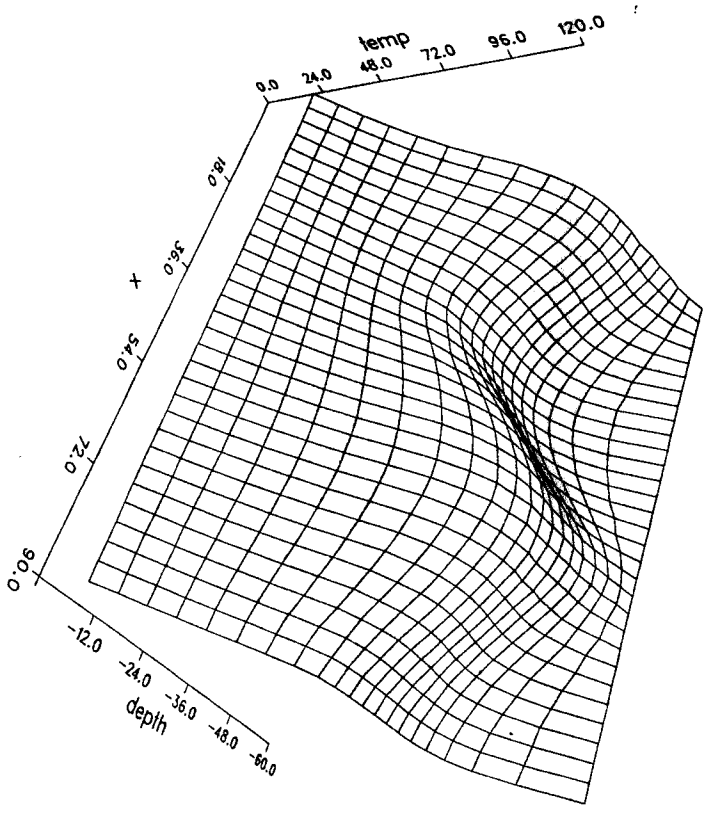
temperature at 30.0 years:  
bottom temperature = 120.0 deg C

Figure 3.3



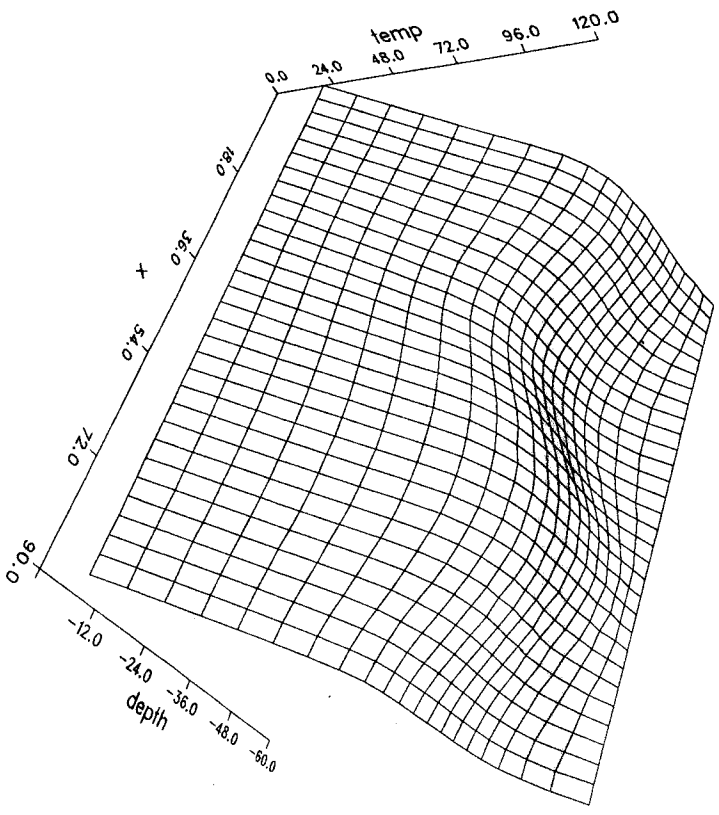
temperature at 42.0 years:  
bottom temperature = 120.0 deg C

Figure 3.4



temperature at 57.0 years  
bottom temperature = 120.0 deg C

Figure 3.5



temperature at 200.0 years  
bottom temperature = 120.0 deg C

Figure 3.6

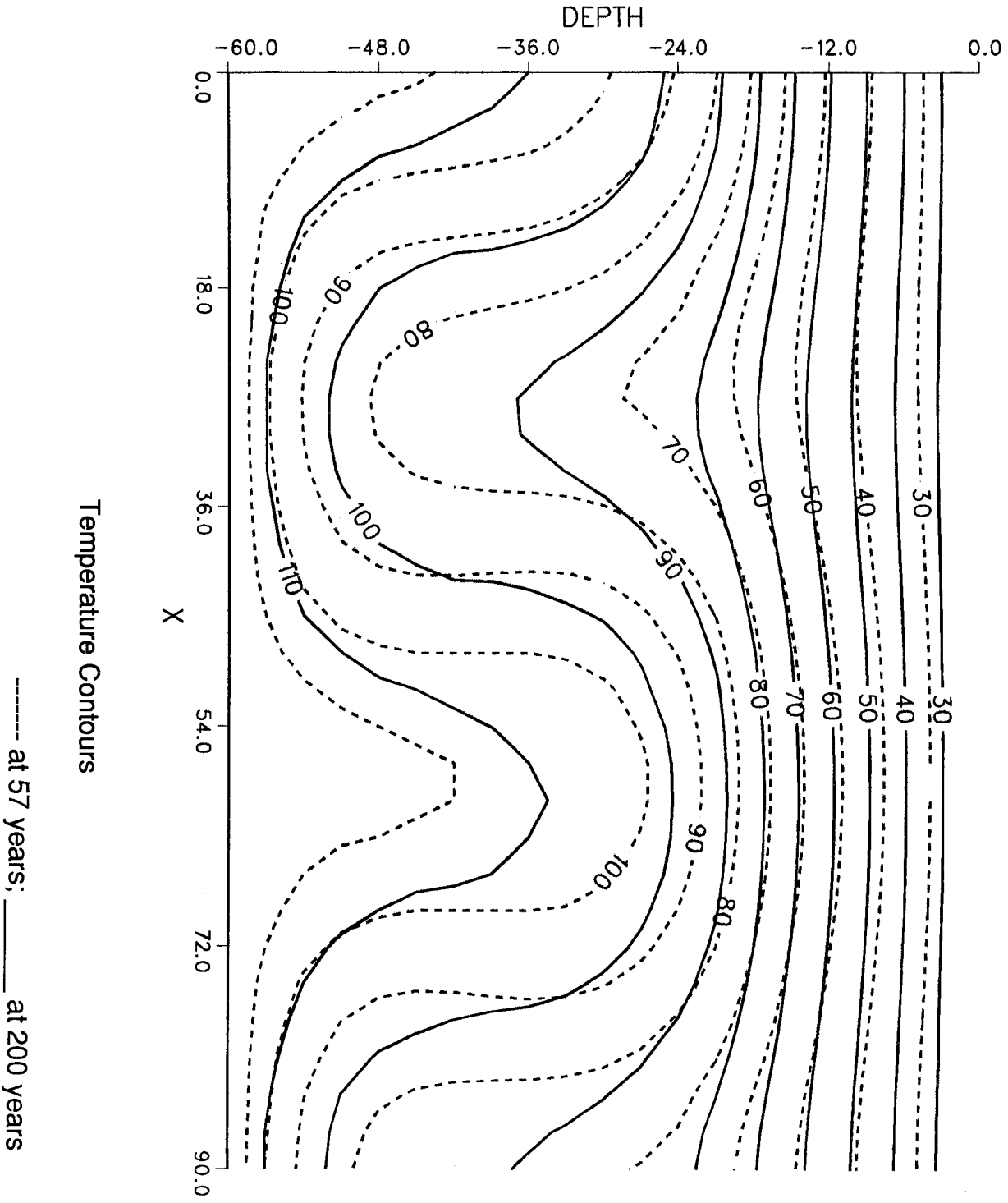
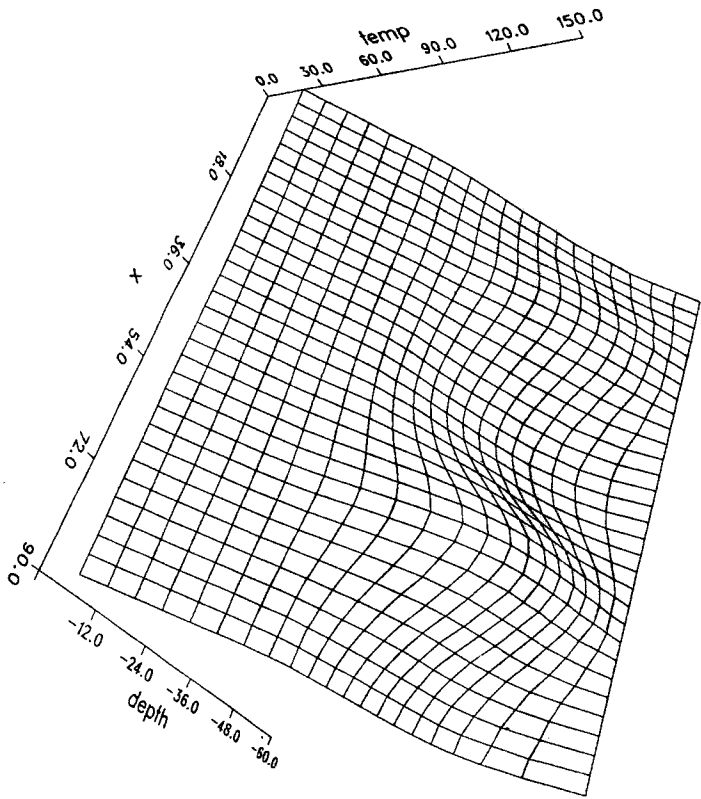
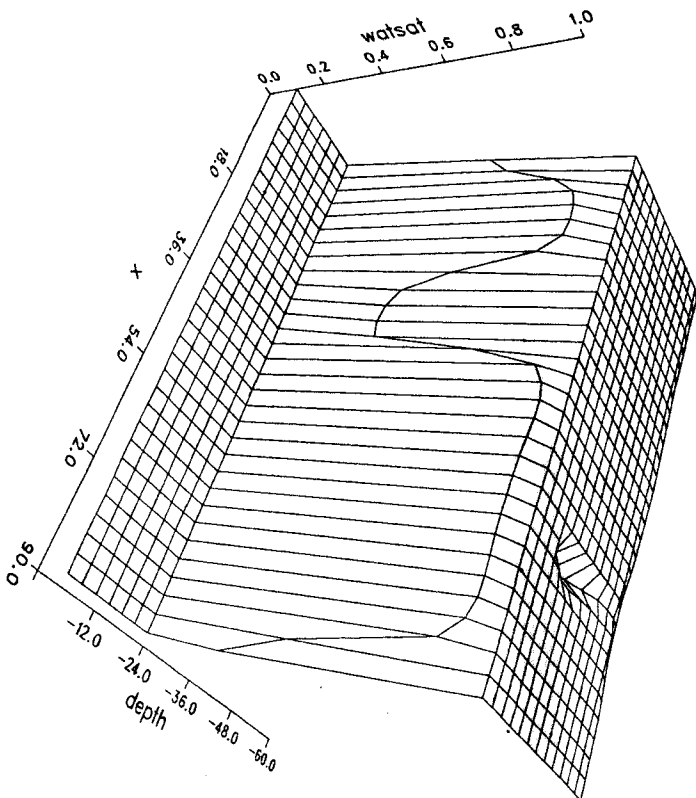


Figure 3.7 (a)



temperature at 24.2 years  
bottom temperature = 150.0 deg C

Figure 3.7 (b)



water saturation at 24.2 years  
bottom temperature = 150.0 deg C

Figure 3.8 (a)

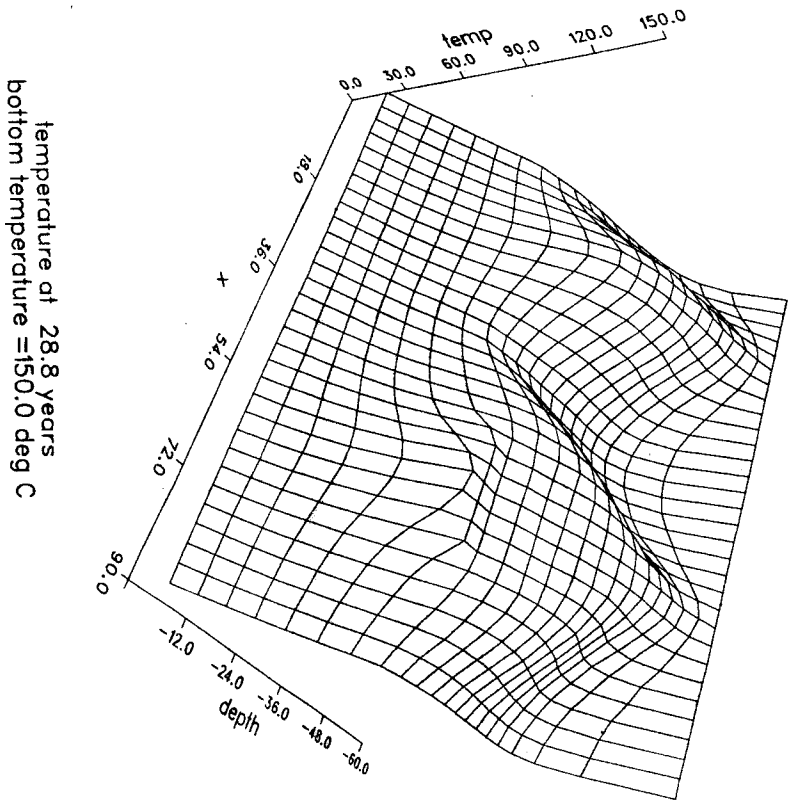


Figure 3.8 (b)

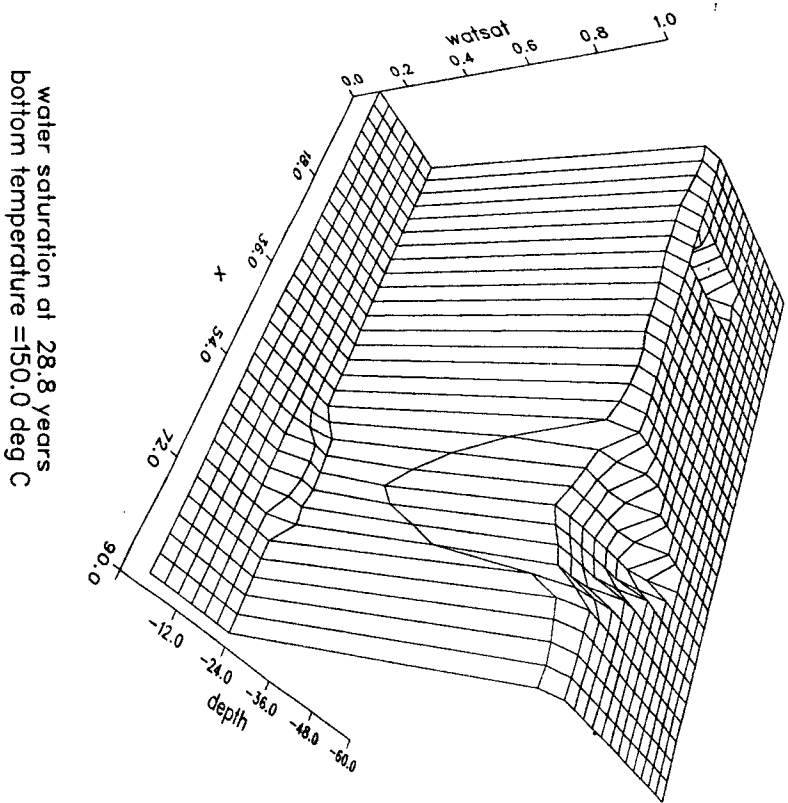




Figure 3.9

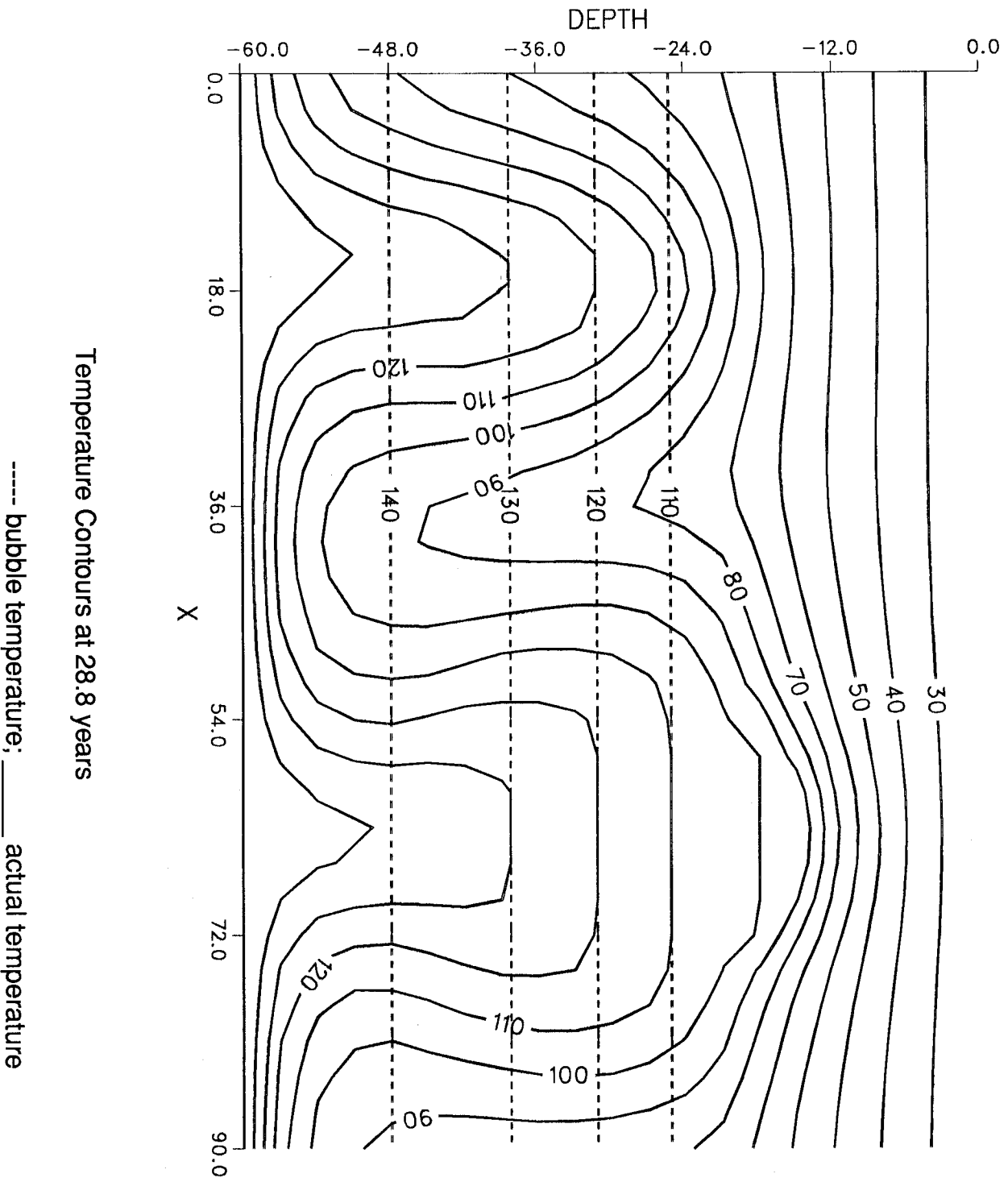


Figure 3.10 (a)

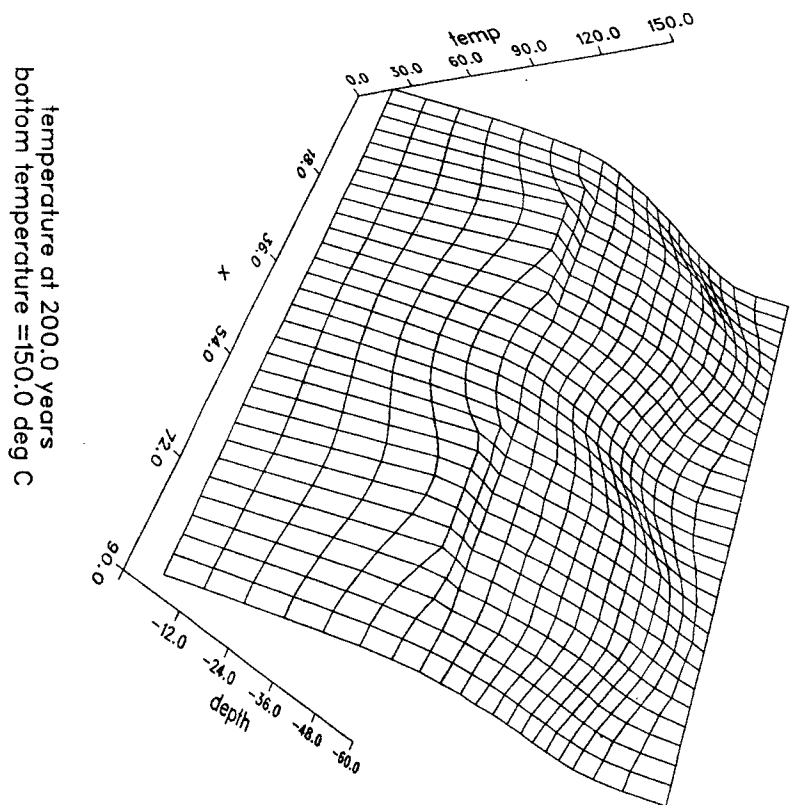


Figure 3.10 (b)

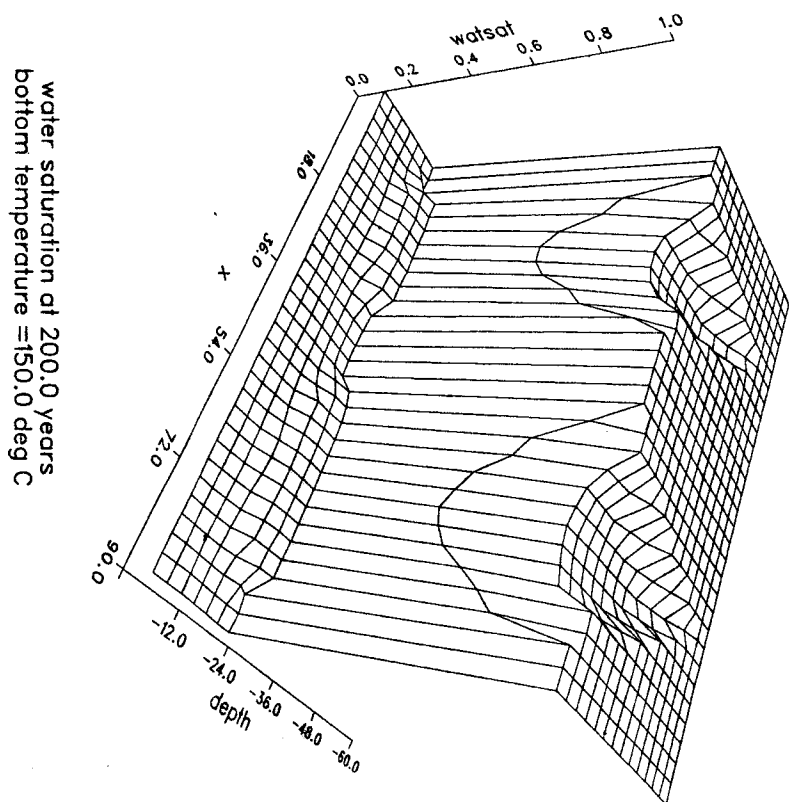


Figure 3.11

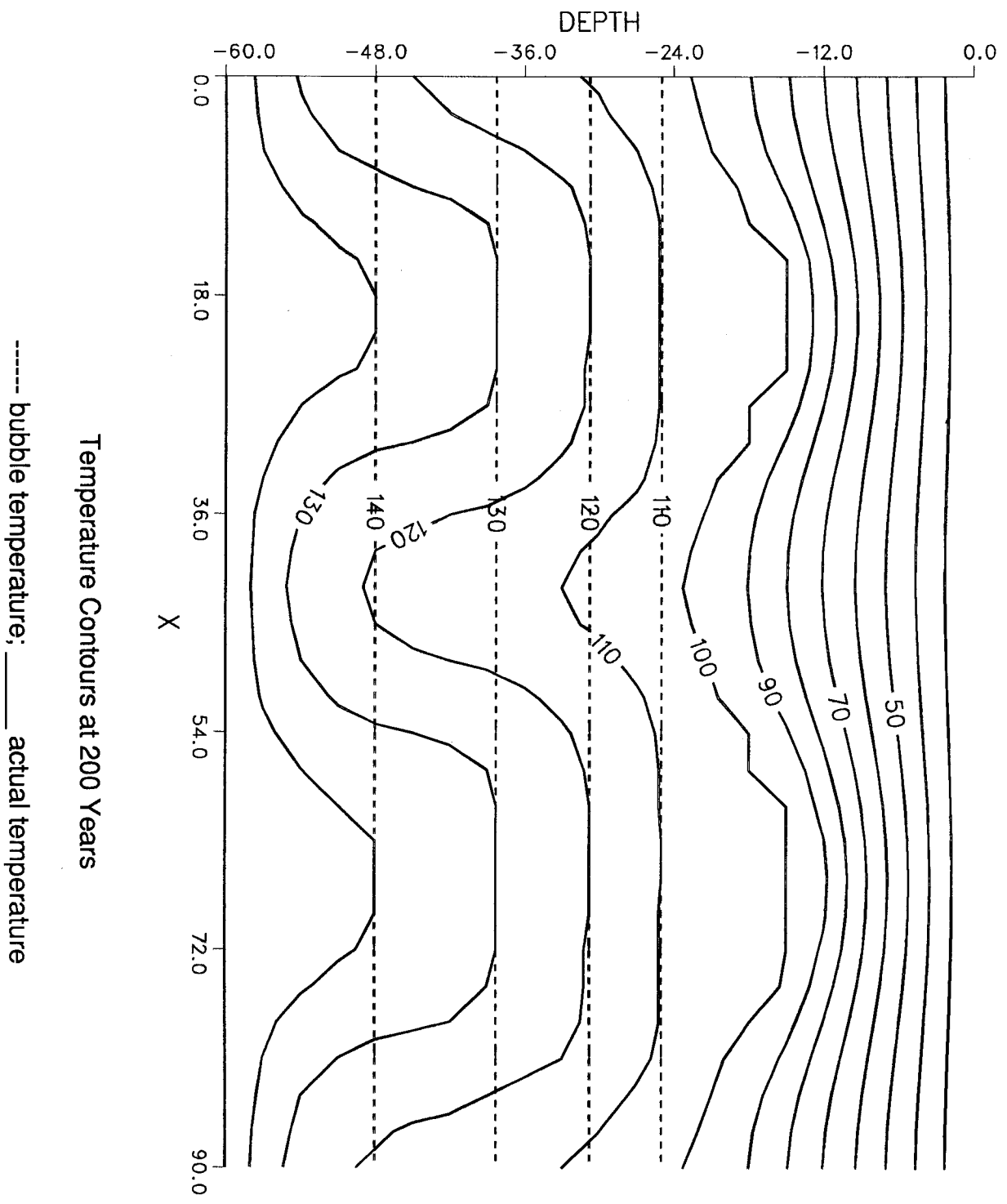


Figure 4.1

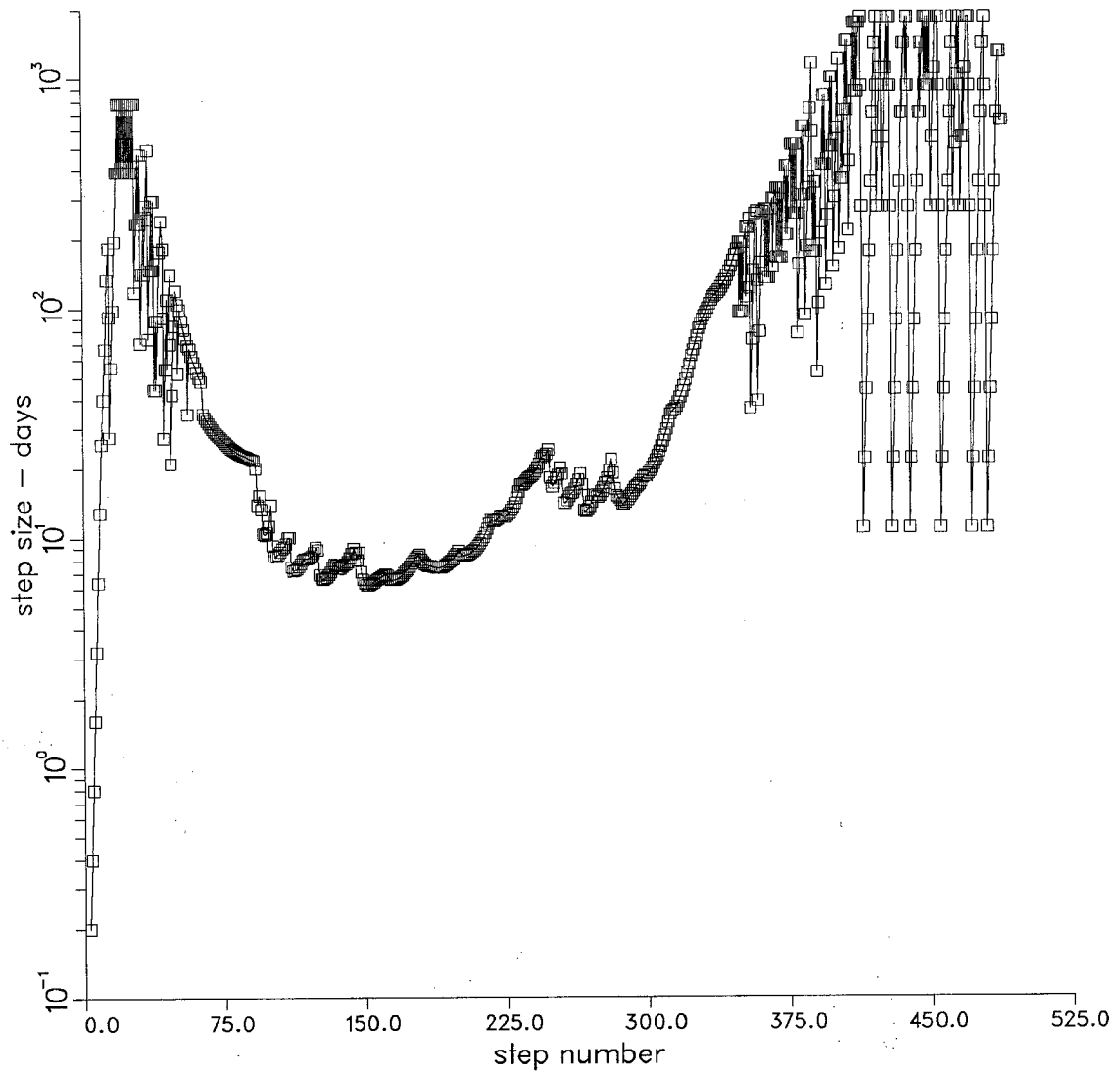


Figure 4.2

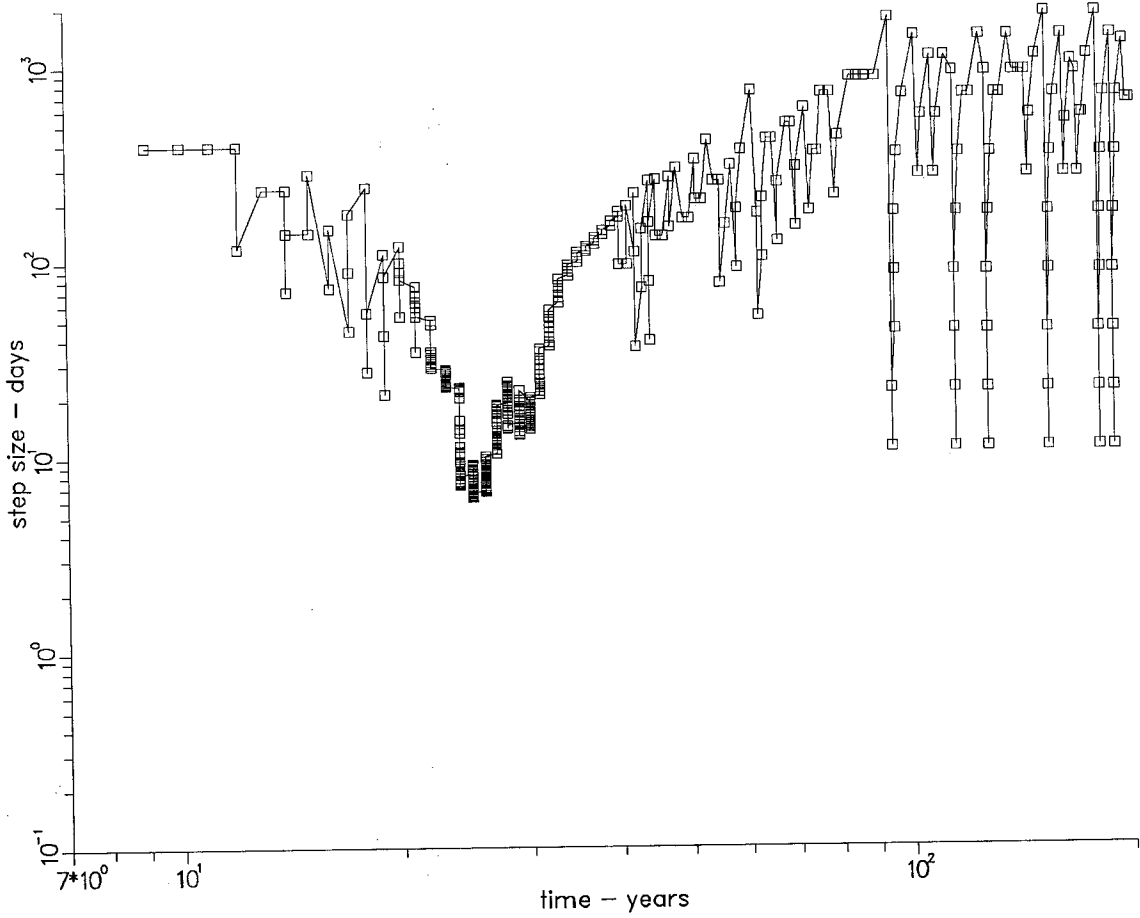
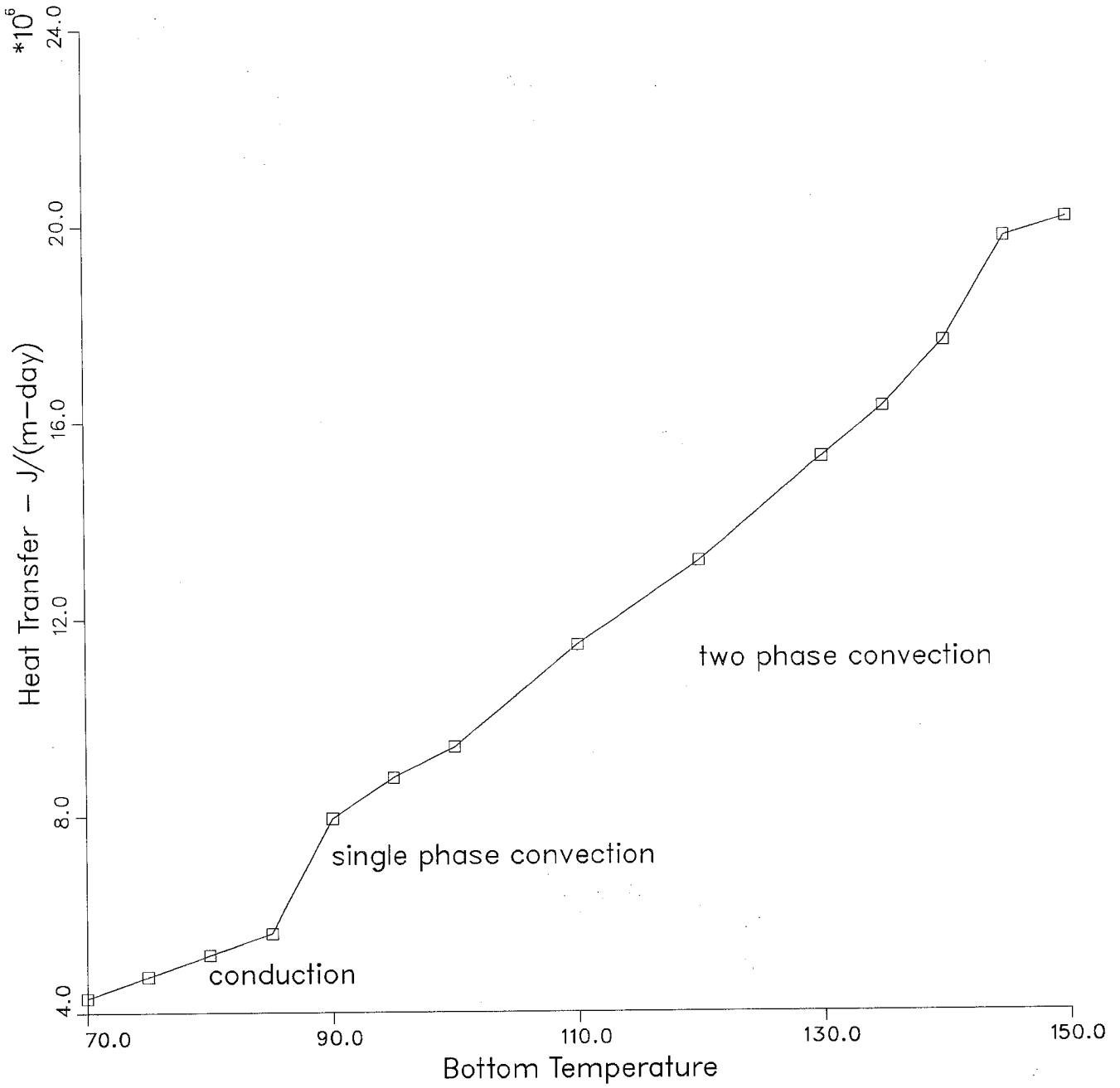


Figure 4.3



**Table 3.1**

Variation of hydrostatic pressure and  $T_{\text{bub}}$  with depth hydrostatic pressure bubble temperature.

$z$ $m$	$P_H$ $Kpa$	$T_{\text{bub}}(P_H)$ $^{\circ}C$
30	197	119.
40	293	133.
50	390	143.
60	486	151.

**Table A.1**

Parameter  $\alpha^*$  for Computing  $Z_a$

$T(^{\circ}K)$	$\alpha^*$
273	30.5
293	19.8
323	13.9

**Table A.2**

**Unsaturated Zone Relative Permeabilities Table**

$S_{\ell}$	$K_{rw}$	$K_{rg}$
0.0	0.0	1.6
.15	0.	1.0
.2	.0002	.83
.4	.02	.35
.6	.148	.104
.8	.447	.013
.9	.68	.001
.95	.83	.0002
1.0	1.0	0.0